Energy Reports 11 (2024) 5602–5618

Contents lists available at ScienceDirect

Energy Reports

journal homepage: www.elsevier.com/locate/egyr

Research paper

Wave energy extraction by an OWC device in the presence of a porous bottom

Nikita Naik [a], Aman Kumar Kushwaha [b], Harekrushna Behera [a,c,*], Chia-Cheng Tsai [c,d,*]

[a] Department of Mathematics, SRM Institute of Science and Technology, Kattankulathur, Chennai 603203, India
[b] Department of Mathematics, Indian Institute of Technology Indore, Indore 453552, India
[c] Center of Excellence for Ocean Engineering, National Taiwan Ocean University, Keelung 202301, Taiwan
[d] Bachelor Degree Program in Ocean Engineering and Technology, National Taiwan Ocean University, Keelung 202301, Taiwan

A R T I C L E I N F O

Keywords:
Wave energy converter
Oscillating water column
Porous bed
Boundary element method
Eigenfunction expansion method

A B S T R A C T

The present study explores the effects of a porous bed on an oscillating water column (OWC) device under the assumptions of the linearized water wave theory and small-amplitude of the surface waves. The velocity potentials in each region have been determined by using the far-field and boundary conditions. To tackle the physical problem, two different mathematical techniques have been employed: the boundary element method (BEM) and the matched eigenfunction expansion method (EEM). The findings of the study are validated by the existing literature. The outcomes of the numerical results and analytical results are in good agreement. It is noted that as the width of the chamber increases, there is an increase in radiation conductance and a decrease in radiation susceptance. The zero efficiencies are observed multiple times as the width of the OWC device increases with respect to the dimensionless wavenumber. Moreover, the study reveals that full efficiency can be obtained by an OWC device over a porous bed for certain wave and structural parameters as obtained in the presence of an impermeable bottom. The proposed model can help to design and develop a successful OWC device.

1. Introduction

Nowadays, there are huge changes in climate and global warming along with the cost of oil becoming high and this led to a boost in government backing, which has played a key role in raising incentives, commercialization, and promoting the use of renewable energy (Boyle, 2008). Among the various renewable energy sources, wave energy has risen as a highly promising choice because of its remarkable advantages. These include minimal harm to the environment, a large amount of energy packed into a small space, and the natural changes in wave energy based on the seasons. These factors work together to provide electricity in a modest climate. Over the past decades for climate change and energy crises, wave energy has drawn more attention and developed more quickly than in the past. However, the levelised cost of energy of wave energy converters (WECs) is still high. The WEC devices are considered to be more prominent in energy conversion. In the past few decades, several physical models have been proposed by many researchers to use as a cost-effective WEC (see, e.g., Kofoed et al. (2006), Babarit et al. (2009) and Haikonen et al. (2013)). Zheng et al. (2022) explained the physical model of the wave power extraction from a floating elastic disc-shaped wave energy converter. In their investigation, the hydroelastic behavior under linearized water wave theory is examined using the eigenfunction expansion method. Recently, Zhu et al. (2023) formulated a physical model to analyze the effectiveness of a hybrid system comprising semi-submersible floating offshore wind turbines (FOWT) assembled in a linear queue of point-absorbing wave energy converters (WECs).

An overview of WEC technology was given by Drew et al. (2009), who divided WECs into two main categories: oscillating bodies and oscillating water columns (OWCs), each of which has distinct characteristics and mechanisms. The OWC has an open-end box made of steel or concrete that is partially immersed in the water and due to the wave action, there is rise and fall in the water on the surface. The detailed wave energy transformation process through an OWC device was discussed by Delmonte et al. (2014) and Doyle and Aggidis (2019), which is highlighted in Fig. 1. The wave energy conversion into electricity involves two stages. In the first stage, the power from the moving water is transformed into mechanical power. This happens when the energy from the waves puts pressure on a fluid, which is then used by an air turbine or Power Take-Off (PTO). After that, in the second stage, the mechanical power is changed into electrical power using a generator. Several mathematical models for wave energy extraction by a single OWC device have been proposed by many researchers (see, e.g., Evans

* Corresponding authors.
E-mail addresses: nikitanaikvssut@gmail.com (N. Naik), amanksept@gmail.com (A.K. Kushwaha), hkb.math@gmail.com (H. Behera), cctsai@mail.ntou.edu.tw (C.-C. Tsai).

https://doi.org/10.1016/j.egyr.2024.05.017
Received 21 September 2023; Received in revised form 21 April 2024; Accepted 11 May 2024
Available online 24 May 2024

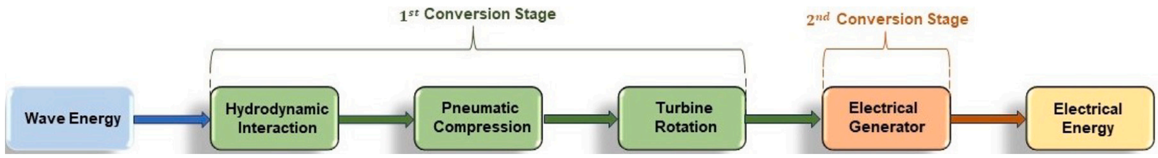

Fig. 1. Wave energy conversion process into electrical energy through the OWC device.
Source: adopted from the works of Delmonte et al. (2014) and Doyle and Aggidis (2019).

and Porter (1995), Morris-Thomas et al. (2007) and Deng et al. (2019)). To explore the wave power extraction by an OWC near the coast with a surging front wall, Deng et al. (2020b) employed the EEM method under the linear wave potential theory. In their findings, the numerical outcomes indicate that the presence of a freely surging lip-wall significantly enhances the device's performance across a broader range of frequencies. Moreover, Deng et al. (2020a) conducted a numerical simulation of a physical model involving an OWC placed over a submerged breakwater. In their study, they employed numerical simulations such as the toolbox waves2Foam and OpenFOAM to analyze the dynamics and performance of this specific configuration. Doyle and Aggidis (2021) experimentally investigated the efficiency of single OWC-WEC and multi OWCs. In their investigation, they demonstrated that the performance of multiple OWC devices is notably influenced by the spacing between the OWC chambers. Recently, Gubesch et al. (2022) examined a design methodology aimed at improving the efficiency of the asymmetrical offshore OWC WEC.

To explore the study focusing on oscillating water column devices Luo et al. (2014) analyzed the mathematical modeling of a floating OWC device in heave mode using the two-dimensional nonlinear computational fluid dynamics model with dynamic mesh. Their findings also showed that the effectiveness of power capture efficiency is notably influenced by both the damping coefficient of the turbine's pneumatic system and the elasticity coefficient of the mooring spring. Moreover, to find the hydrodynamic efficiency of a stationary OWC wave energy device, Ning et al. (2015) constructed a comprehensive nonlinear numerical wave flume (NWF) model in a two-dimensional framework using advanced time-domain higher-order boundary element methodology. Elhanafi and Kim (2018) conducted a combined numerical and experimental investigation into a mathematical model that examined the influence of wave height and power take-off damping on the hydrodynamic performance of an offshore fixed OWC wave energy converter. They revealed that the outcomes obtained from the three-dimensional CFD model exhibited better agreement with experimental results compared to the two-dimensional CFD model. The hydrodynamic performance of an asymmetry OWC device mounted on a box-type breakwater was explained by Deng et al. (2021). They investigated how the width and drafts of the box, as well as the incident wave height, impact the efficiency of wave energy conversion, in addition to analyzing reflection and transmission coefficients. To showcase the hydrodynamic capabilities of a fixed offshore OWC device with a horizontal bottom surface, Deng et al. (2019) performed both numerically and experimentally. For the numerical aspect, they utilized the open-source software package 'OpenFOAM' along with the 'waves2Foam toolbox'. Wang and Zhang (2021) proposed a mathematical model for the efficiency of an OWC device mounted over an immersed horizontal plate. The outcomes of the study reveal that the incorporation of an immersed horizontal plate yields a notable enhancement in the overall performance of the OWC device.

In recent decades, research on the efficiency of multi-chambered OWC devices for wave energy extraction has grown significantly in addition to investigation on single-chambered OWC devices (Rezanejad et al., 2015; Ning et al., 2018; Wang et al., 2021). The advantages of having multiple OWC devices include improved airflow management, more effective energy capture, more flexibility to changing wave conditions, and ultimately higher energy conversion efficiency due to the dynamic interaction between the devices. Haghighi et al. (2021) analyzed the hydrodynamic phenomenon of a dual-chamber OWC and their study reveals that a dual-chamber OWC has a better hydrodynamic efficiency, which is more obvious in small wavelengths. To find the hydrodynamic performance on dual-chamber OWC devices under oblique waves, Li et al. (2022) used the matched eigenfunction expansion. Their investigation revealed that the dual-chamber OWC devices demonstrate an expanded range of capture bandwidth in comparison to a single-chamber OWC. Wang and Zhang (2022) formulated the performance capability for a dual-chambered OWC conceived from wall effects in narrow flumes and showed how the harbor walls enhance the wave power extraction.

In the aforementioned studies, the bottom of the sea was assumed to be rigid. However, in real cases, the seabed is quite different. The seabed is not a rigid, immovable surface; instead, it is porous, sloping, and slippery. Several studies have explored the phenomenon of wave scattering by various breakwaters over an uneven rigid bottom (Dong et al., 2018; Chang and Tsai, 2022; Tsai et al., 2022). On the other hand, the porous bed absorbs the wave energy and the utilization of a porous bed gives a boundary condition on the seabed that includes a porous effect parameter. In recent decades, several mathematical models have been developed by many researchers to evaluate the effectiveness of porous seabed on wave scattering and trapping by various coastal structures of different configurations in single/two-layer fluid (see, e.g., Martha et al. (2007), Maiti and Mandal (2014), Behera et al. (2018) and Chanda and Bora (2020)). Their study shows that the porous bed absorbs a significant amount of wave energy and results in lesser wave transmission. Sarkar and Chanda (2022) investigated a study examining the structural behavior of a submerged compound porous cylinder mounted at the bottom, focusing on its interaction with water waves in the context of a permeable seabed. They revealed that the compound cylinder is more effective in reducing the impact of waves when porosity and structural factors are appropriately taken into account.

Since a porous bottom greatly affects wave dynamics and as far as the authors are aware, no theoretical research has been done on how a porous bottom affects the efficiency of single or multiple OWCs in the literature, they were motivated to examine how a flat porous bottom affects OWC efficiency. It is important to highlight that we have not considered the motion of the fluid inside the flat porous bed by following the work of Maiti and Mandal (2014). This investigation has been done by both an analytical approach employing the eigenfunction expansion method (EEM) and a numerical technique utilizing the boundary element method (BEM). A detailed summary of a few previous studies and present work is highlighted in Table 1 along with their methodologies to tackle the physical model, nature of bottom topography, and number of OWC. This comparison table shows the novelty of the present study.

The remainder of this paper is structured as follows. The complete description of a problem formulation along with the governing equation is described in Section 2. Section 3 illustrates the concept of solving the mathematical model utilizing the EEM and BEM. The parameters pertaining to the performance of the OWC device are elucidated in Section 4. In Section 5, the present theory is validated with existing results available in the literature, the results obtained by both analytical and numerical methods are compared, and the effectiveness of the porous bed is investigated with different physical parameters for an effective OWC. The conclusion of this work is presented in Section 6.

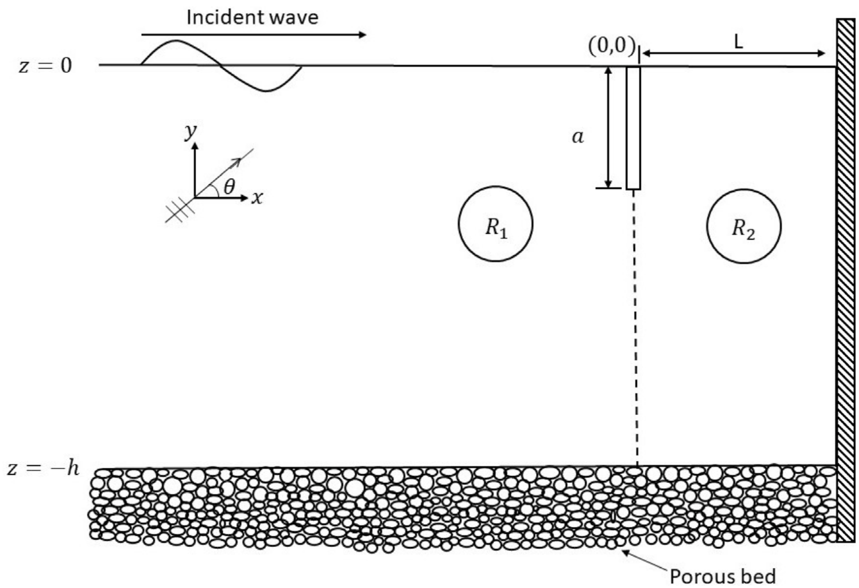

Fig. 2. Schematic depiction of single chambered OWC over a porous bed for EEM.

Table 1
Summary of the past investigations for single/dual/multiple OWC devices along with the present model.

Author's name	No. of OWC	Types of bottom	Methodology
Rezanejad et al. (2013)	Single	Stepped rigid	EEM
Koley and Trivedi (2020)	Single	Undulated rigid	BEM
He et al. (2019)	Single	Flat rigid	EEM
Naik et al. (2023a)	Dual	Undulated rigid	BEM
Zheng et al. (2020)	Multiple	Flat rigid	EEM
Present model	Single	Flat porous	EEM & BEM

2. Mathematical formulation

In this section, we provide a comprehensive explanation of the present study, demonstrating how it can be tackled through both numerical and analytical methods. We consider an OWC device placed over a porous bed of sea/ocean as shown in both Figs. 2 and 3. The relevant physical model is explained by employing a three-dimensional cartesian coordinate system (x, y, z) where the x-y plane lies on the horizontal surface while the positive z-axis extends vertically in an upward direction. The parameter θ represents the angle of the oblique wave with x-axis in both Figs. 2 and 3. The eigenfunction expansion technique is employed for the analytical solution, whereas the numerical solution is obtained by the boundary element method. The detailed problem description along with the governing equation, boundary conditions, and solutions are discussed in the subsequent sections separately.

2.1. Problem description: EEM

To tackle the present physical model analytically, the eigenfunction expansion method is used and the schematic representation is shown in Fig. 2. The water depth from the seabed to the mean free surface of water is h. The distance between the vertical barrier and the rigid wall is denoted by L. The complete fluid domain is divided into two distinct regions namely: R_1 and R_2. These regions are precisely defined as follows: $R_1 = \{x \mid -\infty < x < 0\}$ and $R_2 = \{x \mid 0 < x < L\}$. The present setup is modeled as a surface-piercing thin rigid vertical barrier with height a and placed at $(x, y) = (0, 0)$, near a rigid wall, and L denotes the width of the OWC chamber.

2.2. Problem description: BEM

The same physical model as in Fig. 2, is tacked using the boundary element method. The schematic diagram for BEM is shown in Fig. 3. To apply the BEM, we bound the whole domain by L_i (for $i = 1, 2, \ldots, 8$). The auxiliary boundary is fixed at $x = -r_0$. The whole domain is classified into two regions, say R_{open} and R_{inner}. These regions are precisely defined by $R_{open} = \{(x, y) \in L_1 \cup L_2 \cup L_3 \cup L_4 \cup L_5\}$ and $R_{inner} = \{(x, y) \in L_4 \cup L_3 \cup L_6 \cup L_7 \cup L_8\}$ where $L_1 = \{z \mid -h < z < 0, x = -r_0\}$; $L_2 = \{x \mid -r_0 < x < 0, z = -h\}$; $L_3 = \{z \mid -h < z < -h + a, x = 0\}$; $L_4 = \{z \mid -a < z < 0, x = 0\}$; $L_5 = \{x \mid -r_0 < x < 0, z = 0\}$; $L_6 = \{x \mid 0 < x < L, z = -h\}$; $L_7 = \{z \mid -h < z < 0, x = L\}$ and $L_8 = \{x \mid 0 < x < L, z = 0\}$. The notations L_6 and L_8 both denote the gap between the barrier and the rigid wall and are equal to L as in Fig. 2.

2.3. Governing equation and boundary conditions

The fluid is supposed to be inviscid and incompressible with an irrotational motion of the flow. Due to the irrotational nature of the flow, the velocity potential $\Phi(x, y, z, t)$ corresponding to each velocity component always exists. In the case of the fluid, the motion is always supposed to be a simple harmonic motion with angular frequency ω. Therefore, the velocity potential $\Phi(x, z, t)$, which can be written as $\Re\{\phi_j(x, z)e^{-\mathrm{i}(k_y y - \omega t)}\}$ $(j \in 1, 2)$, where $\Re$ denotes the real part of a complex number; $\phi_j(x, z)$ is the complex-valued spatial velocity potential independent with time t; $k_y = k_0 \sin\theta$ and k_0 is the progressive wave number of the incident wave. Owing to the nature of incompressibility, the continuity equation yields the governing equation which is the Helmholtz equation and is expressed in the Cartesian coordinate system as

$$\left(\frac{\partial}{\partial_{xx}} + \frac{\partial}{\partial_{zz}} - k_y^2\right)\phi_j = 0 \quad \text{for } j = 1, 2. \tag{1}$$

According to the work done by Naik et al. (2023b), the total velocity potential reads

$$\phi_j = \phi_j^S + \phi_j^R, \quad \text{for all } j, \tag{2}$$

where the radiated and scattered velocity potentials are denoted by ϕ_j^R and ϕ_j^S, respectively. The mean free surface boundary conditions

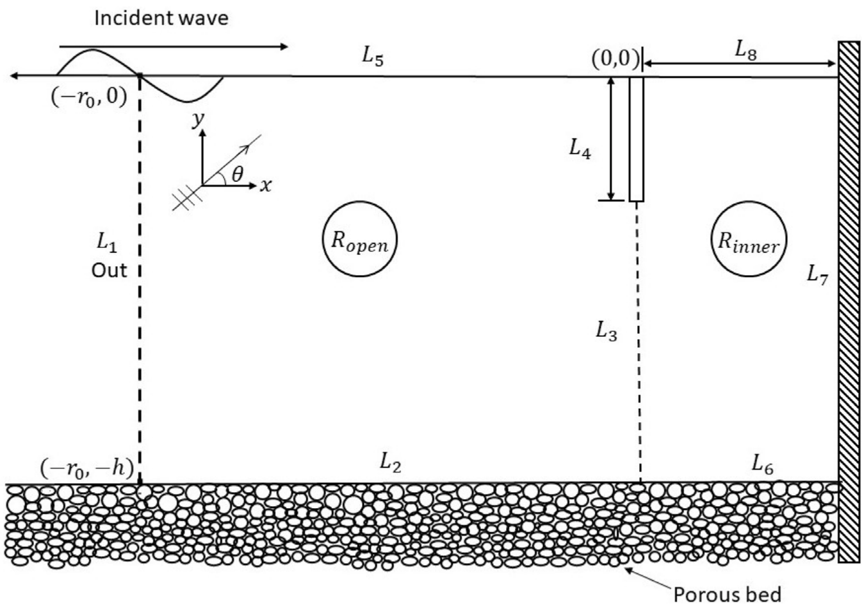

Fig. 3. Schematic depiction of single chambered OWC over a porous bed for BEM.

under the linearized water wave theory for the scattered and radiated velocity potentials are given as (He et al., 2019),

$$\frac{\partial \phi_1^{S,R}}{\partial z} + K\phi_1^{S,R} = 0 \quad \text{at } L_5, \tag{3}$$

$$\frac{\partial \phi_2^{S,R}}{\partial z} + K\phi_2^{S,R} = -\frac{\mathrm{i}\omega\delta_{l,2}}{\rho g} \quad \text{at } L_8 \quad \text{at for } i = 1,2 \tag{4}$$

where $K = \omega^2/g$ and g represents the gravitational acceleration and $\delta_{l,2}$ is the Kronecker delta function. Eq. (4) defines the boundary condition for the scattered and radiated velocity potentials, respectively, for $l = 1$ and $l = 2$. The pressure distribution across the inner free surface for OWC is expressed as follows:

$$\mathcal{P}(t) = \Re\{pe^{-\mathrm{i}\omega t}\} \tag{5}$$

where p represents the pressure inside the OWC chamber. The vertical panel resembling the oscillating water column is also impenetrable, and the associated boundary condition is given by,

$$\frac{\partial \phi_j^{S,R}}{\partial n} = 0, \quad \text{at } L_4 \text{ and } L_7 \quad \text{for } j = 1,2. \tag{6}$$

Furthermore, at $x = 0$, the velocity and pressure continuities in the region $L_3 = -h \leq z \leq -L_4$ read,

$$\frac{\partial \phi_1^{S,R}}{\partial x} = \frac{\partial \phi_2^{S,R}}{\partial x}, \quad \phi_1^{S,R} = \phi_2^{S,R}. \tag{7}$$

The linearized boundary condition on the porous seabed is given by Behera et al. (2018) and Barman and Bora (2022)

$$\frac{\partial \phi_j^{S,R}}{\partial z} - G\phi_j^{S,R} = 0 \quad \text{at } L_2, \ \ L_6 \quad \text{for} \quad j = 1,2, \tag{8}$$

where G presents the porous effect parameter.

Furthermore, The far-field conditions for the numerical computations are governed by,

$$\phi_1^R(x,z) = \mathcal{A}_0^R e^{-\mathrm{i}\mu_0(x+r_0)} f_0(z), \quad x \to -\infty, \tag{9}$$

$$\phi_1^S(x,z) = (I_0 e^{\mathrm{i}\mu_0(x-L)} + \mathcal{A}_0^S e^{-\mathrm{i}\mu_0(x+r_0)}) f_0(z), \quad x \to -\infty, \tag{10}$$

where, I_0, $\mathcal{A}_0^S$ and $\mathcal{A}_0^R$ signify the incident, reflected, and radiated wave amplitudes, respectively.

3. Solution methodology

3.1. Analytical solution by EEM

This subsection provides the approach for finding solutions to the scattered and radiated velocity potentials using the matched EEM.

3.1.1. Radiated velocity potential

The velocity potential in region 1 ($-\infty < x < 0, \ -h < z < 0$) and region 2 ($0 < x < L, \ -h < z < 0$), is the solution of the governing Eq. (1), satisfying the boundary conditions (3) and (8) are obtained as Zheng et al. (2020)

$$\phi_1^R = \sum_{n=0}^{\infty} A_n^R e^{-i\mu_n x} f_n(z) \quad \text{for region 1}, \tag{11}$$

$$\phi_2^R = \sum_{n=0}^{\infty} B_n^R \cosh \mu_n (x - L_8) f_n(z) - \frac{\mathrm{i}}{\rho\omega} \quad \text{for region 2}, \tag{12}$$

where A_n^R and B_n^R are the unknown coefficients; $\mu_n = \sqrt{{k_n}^2 - {k_y}^2}$ (for $n = 0,1,2,\ldots$); $f_n(z)$ (for $n = 0,1,2,\ldots$) are the eigenfunctions, given by Behera et al. (2018) and Barman and Bora (2022)

$$f_n(z) = \left(\frac{\mathrm{i}g}{\omega}\right) \frac{k_n \cosh(k_n(z+h)) - G\sinh(k_n(z+h))}{k_n \cosh(k_n h) - G\sinh(k_n h)} \tag{13}$$

and k_n (for $n = 0,1,2,\ldots$) are the wavenumbers that satisfy the dispersion relation in the open water region, described as

$$k_n(k_n \tanh k_n h - G) = K(k_n - G\tanh k_n h). \tag{14}$$

It is worthwhile mentioning that in the present work, for $G = 0$, the porous bed becomes a rigid bed then the dispersion relation is similar to He et al. (2019), Rodríguez et al. (2022), and references therein. The velocity potentials defined in Eqs. (11) and (12) are substituted into Eqs. (6) and (7) then we use the orthogonality of the eigenfunctions in the region $[-h, 0]$. The obtained system of infinite linear equations is obtained as

$$\sum_{n=0}^{\infty} -i\mu_n A_n^R X_{nq} - \sum_{n=0}^{\infty} B_n^R \mu_n \sinh \mu_n(L_8) Y_{nq} = 0, \tag{15}$$

$$\sum_{n=0}^{\infty} A_n^R Y_{nq} - \sum_{n=0}^{\infty} B_n^R \cosh \mu_n(L_8) Y_{nq} = -\frac{\mathrm{i}}{\rho\omega} M_q, \tag{16}$$

where

$$X_{nq} = \int_{-h}^{0} f_0(z) f_q(z) dz, \quad Y_{nq} = \int_{-h}^{-L_4} f_n(z) f_q(z) dz,$$
$$M_q = \int_{-h}^{-L_4} f_q(z) dz.$$

for $n, q = 0, 1, 2, \ldots$. To find the unknown coefficients A_n^R and B_n^R involved in the system of Eqs. (15) and (16), any numerical technique can be utilized to solve these unknowns. However, in practical scenarios, we can handle only a finite number of unknowns. Therefore, to address this limitation, the series in Eqs. (15) and (16) are truncated at a reasonable value for n, denoted as N. Consequently, the system of equations involves a total of $2(N+1)$ unknown coefficients. The complete velocity potentials in each region have been determined to evaluate the efficiency, radiation susceptance, and radiation conductance of the OWC device.

3.1.2. Scattered velocity potential

The scattered velocity potentials are given by

$$\phi_1^S = I_0 e^{\mathrm{i}\mu_0 x} f_0(z) + \sum_{n=1}^{\infty} A_n^S e^{-\mathrm{i}\mu_n x} f_n(z) \quad \text{for region 1,} \tag{17}$$

$$\phi_2^S = \sum_{n=0}^{\infty} B_n^S \cosh \mu_n (x - L_8) f_n(z) \quad \text{for region 2,} \tag{18}$$

Continuing with a similar process as used for the velocity potential of radiated waves, and applying the matching conditions along with the orthogonality condition, a system of infinite linear equations is obtained by

$$\sum_{n=1}^{\infty} -\mathrm{i}\mu_n A_n^S X_{nq} - \sum_{n=0}^{\infty} B_n^S \mu_n \sinh \mu_n (L_8) Y_{nq} = -\mathrm{i} I_0 \mu_0 X_{0q}, \tag{19}$$

$$\sum_{n=1}^{\infty} A_n^S Y_{nq} - \sum_{n=0}^{\infty} B_n^S \cosh \mu_n (L_8) Y_{nq} = -Y_{0q} \tag{20}$$

Once the values of the unknown coefficients A_n^S and B_n^S are ascertained, the entire radiated velocity potential is established. Following a similar process in radiated velocity potential, the total efficiency of the system is found.

3.2. Numerical solution by BEM

By employing Green's theorem for the integral to Eq. (1) and making use of Green's function $\mathcal{G}$, we can formulate the subsequent integral equation in the following manner:

$$-\begin{pmatrix} \phi(\zeta,\eta) \\ \frac{1}{2}\phi(\zeta,\eta) \end{pmatrix} = \int_{\Gamma} \left(\phi \frac{\partial \mathcal{G}}{\partial \mathbf{n}}(x,z;\zeta,\eta) - \mathcal{G}(x,z;\zeta,\eta) \frac{\partial \phi}{\partial \mathbf{n}} \right) d\Gamma,$$
$$\begin{pmatrix} \text{if } (x,z) \in \text{int}(\Gamma) \\ \text{if } (x,z) \in \Gamma \end{pmatrix}. \tag{21}$$

Here, the mentioned (ζ, η) represents the source point, located on the boundary Γ, while (x, z) corresponds to the field point. Additionally, $\mathbf{n}$ denotes the outward normal vector. Furthermore, to evaluate the Green's function, the elementary solution of the equation is provided as follows:

$$(\nabla^2 - k_y)\mathcal{G} = \delta(\zeta - x)\delta(\eta - z);$$
$$\mathcal{G}(x,z;\zeta,\eta) = \frac{\zeta_0(k_y r)}{2\pi} \quad \text{where} \quad r = \sqrt{(\zeta - x)^2 + (\eta - z)^2}. \tag{22}$$

In Eq. (22), the symbol ζ denotes the modified-zeroth order Bessel function of the first kind. As r approaches zero, the asymptotic behavior is given by

$$\psi_0(k_y r) = -\lambda - \ln\left(\frac{k_y r}{2}\right), \tag{23}$$

where λ signifies the Euler's constant which has a numerical value of approximately 0.5772. After applying the boundary conditions along with the porous effect in the region R_{open} and R_{inner} (as shown in Fig. 3), we proceed with the velocity potential as a constant value along each of the boundary components. This leads to the corresponding system of integral equations:

$$\beta\phi_1 + \int_{L_1} \left(\phi_1 \frac{\partial \mathcal{G}}{\partial n} - \mathcal{G}\frac{\partial \phi_1}{\partial n} \right) dL + \int_{L_2} \left(\phi_1 \frac{\partial \mathcal{G}}{\partial n} - \mathcal{G}G\phi_1 \right) dL$$
$$+ \int_{L_3} \left(\phi_1 \frac{\partial \mathcal{G}}{\partial n} - \mathcal{G}\frac{\partial \phi_1}{\partial n} \right) dL + \tag{24}$$
$$\int_{L_4} \phi_1 \frac{\partial \mathcal{G}}{\partial n} dL + \int_{L_5} \left(\phi_1 \frac{\partial \mathcal{G}}{\partial n} + K\mathcal{G}\phi_1 \right) dL = 0,$$

$$\beta\phi_2 + \int_{L_4} \phi_2 \frac{\partial \mathcal{G}}{\partial n} dL + \int_{L_3} \left(\phi_2 \frac{\partial \mathcal{G}}{\partial n} - \mathcal{G}\frac{\partial \phi_2}{\partial n} \right) dL + \int_{L_6} \left(\phi_2 \frac{\partial \mathcal{G}}{\partial n} - \mathcal{G}G\phi_2 \right) dL$$
$$+ \int_{L_7} \phi_2 \frac{\partial \mathcal{G}}{\partial n} dL +$$
$$\int_{L_8} \left(\phi_2 \frac{\partial \mathcal{G}}{\partial n} + K\mathcal{G}\phi_2 + \mathcal{G}\frac{\mathrm{i}\omega\delta_{l,2}}{\rho g} \right) dL = 0, \tag{25}$$

where $\beta = 1/2$. Eqs. (24) and (25) represent the system of integral equations for the scattered and radiated velocity potentials, respectively, for $l = 1$ and $l = 2$. Next Eqs. (24) and (25) can be written as algebraic system of equations:

$$\sum \left(\phi_{1j} M^{ij} - N^{ij} \frac{\partial \phi_{1j}}{\partial n} \right) \Big|_{L_1} + \sum \left(\phi_{1j} M^{ij} - N^{ij} G\phi_{1j} \right) \Big|_{L_2}$$
$$+ \sum \left(\phi_{1j} M^{ij} - N^{ij} \frac{\partial \phi_{1j}}{\partial n} \right) \Big|_{L_3} +$$
$$\sum \left(\phi_{1j} M^{ij} \right) \Big|_{L_4} + \sum \left(\phi_{1j} M^{ij} - K N^{ij} \phi_{1j} \right) \Big|_{L_5} = 0, \tag{26}$$

$$\sum \left(\phi_{2j} M^{ij} \right) \Big|_{L_4} + \sum \left(\phi_{2j} M^{ij} - N^{ij} G\phi_{2j} \right) \Big|_{L_3}$$
$$+ \sum \left(\phi_{2j} M^{ij} - G N^{ij} \phi_{2j} \right) \Big|_{L_6} +$$
$$\sum \left(\phi_{2j} M^{ij} \right) \Big|_{L_7} + \sum \left(\phi_{2j} M^{ij} + K N^{ij} \phi_{2j} + N^{ij} \frac{\mathrm{i}\omega}{\rho g} \delta_{l,2} \right) \Big|_{L_8} = 0, \tag{27}$$

where $M^{ij} = \frac{1}{2}\delta_{i,j} + \int_{L_i} \frac{\partial \mathcal{G}}{\partial n} dL_i$ and $N^{ij} = \int_{L_i} \mathcal{G} dL_i$. To find the unknown coefficients in the above system of Eqs. (26) and (27), the numerical integration is used. After putting all unknown coefficients into Eqs. (11)–(12) and Eqs. (17)–(18), the radiated and scattered velocity potentials are obtained, respectively.

4. OWC governing parameters

This section presents the mathematical formulas describing various physical parameters relevant to the operation of the OWC device. The volume flux across the internal free surface is calculated by following the method described in the work of Naik et al. (2023b), which is given by

$$q = \int_{L_8} \frac{\partial \phi}{\partial z} dx = q^S - \frac{\mathrm{i}\omega p}{\rho g} q^R, \tag{28}$$

where the notations q^S and q^R are used to represent the volume flow rates over the internal free surfaces (L_8) for the scattering and radiation problems, respectively. The volume flow rate required for the radiation potential is expressed as follows:

$$\frac{\mathrm{i}\omega p}{\rho g} q^R = (\tilde{\beta} - \mathrm{i}\tilde{\alpha})p. \tag{29}$$

In Eq. (29), the expressions $\tilde{\beta}$ and $\tilde{\alpha}$ are referred to as the radiation susceptance and radiation conductance of the OWC device, respectively. These expressions, $\tilde{\beta}$ and $\tilde{\alpha}$, are akin to added mass and damping coefficient. To find $\tilde{\beta}$ and $\tilde{\alpha}$, we use

$$\tilde{\alpha} = \frac{\omega}{\rho g}\Re\{q^R\}, \quad \tilde{\beta} = \frac{\omega}{\rho g}\Im\{q^R\}, \tag{30}$$

where, $\Im$ and $\Re$ denote the imaginary and real components of the complex number, respectively. It is hypothesized that the amount of fluid passing through the turbine is directly related to the decrease in pressure across the inner free surface and expressed as,

$$q = \Lambda p, \tag{31}$$

where Λ represents the positive real constant, which is known as a control parameter. In addition to the volume flux, the average rate of work performed by the pressure over a single wave period is defined by Khan and Behera (2021),

$$W = \frac{|q_s|^2}{2}\frac{\Lambda}{(\Lambda+\tilde{\beta})^2+\tilde{\alpha}^2}, \tag{32}$$

Referring to the known values of $\tilde{\alpha}$ and $\tilde{\beta}$, the established optimum value is given by,

$$\Lambda_{opt} = \sqrt{\tilde{\alpha}^2+\tilde{\beta}^2}, \tag{33}$$

Therefore, the highest amount of work accomplished by pressure during a single period is obtained by,

$$W_{max} = \frac{|q_s|^2}{4}\frac{1}{\Lambda_{opt}+\tilde{\beta}}, \tag{34}$$

For a plane progressive wave with unit amplitude, the available power over one wave period is given by Trivedi and Koley (2022) and Naik et al. (2023a),

$$\mathcal{P}_W = \mathscr{E}_W c_g = \frac{\rho\omega k_0 \psi_0}{2}, \quad \psi_0 = \int_{-h}^{0} f_0^2(z)dz, \tag{35}$$

where c_g is the group velocity and $\mathscr{E}_W$ stands for the total energy per wave period. The efficiency of OWC is given by,

$$\eta_{max} = \frac{W_{max}}{\mathcal{P}_W}, \tag{36}$$

The dimensionless parameters μ and ν are employed as the symbol of radiation susceptance and radiation conductance, respectively, which are given by

$$\mu = \frac{\rho g}{\omega L}\tilde{\alpha}, \quad \nu = \frac{\rho g}{\omega L}\tilde{\beta}, \tag{37}$$

The total efficiency of the system is defined as follows,

$$\eta = \frac{2}{\left(1+\left(\frac{\mu}{\nu}\right)^2\right)^{\frac{1}{2}}+1}. \tag{38}$$

5. Results and discussion

This section presents numerous outcomes regarding the performance of an OWC device. All the numerical computations are performed by the Matlab® software. The results for radiation conductance and radiation susceptance along with efficiency have been plotted and discussed. Furthermore, it is important to note that several resonance mechanisms occurring within the OWC device play a substantial role in determining the efficiency of the OWC device (see, e.g., Rezanejad et al. (2013) and Trivedi and Koley (2021)). The following physical quantities have been chosen for the remainder of the study for computation, such as water depth, $h = 4$m; barrier length, $a/h = 0.4$; distance between auxiliary boundary and barrier, $L_2/h = 1$; OWC chamber width, $L/h = 1$; oblique angle, $\theta = 20°$; incident wave amplitude, $I_0 = 1$m and porosity of the bottom, $Gh = 0.8$ unless it is highlighted in the appropriate figure's caption.

Table 2
Comparative study of the efficiency (η), radiation susceptance (μ) and radiation conductance (ν) for a/h =0.2, 0.5 & 0.8 with $L/h = 1$, $\theta = 20°$, $k_0h = 1.2$ and $Gh = 0.8$.

N	a/h	Analytic solution (EEM)			Numerical solution (BEM)		
		η	μ	ν	η	μ	ν
1	0.2	0.9650	0.5142	1.3264	0.9543	0.5047	1.3056
	0.5	0.9829	0.2339	0.8798	0.9730	0.2254	0.8671
	0.8	0.9961	0.0454	0.3632	0.9853	0.0295	0.3558
3	0.2	0.9740	0.4873	1.2880	0.9691	0.4728	1.2794
	0.5	0.9783	0.2518	0.8552	0.9720	0.2478	0.8429
	0.8	0.9852	0.0256	0.3759	0.9817	0.0198	0.3680
5	0.2	0.9774	0.5037	1.3089	0.9675	0.4890	1.2987
	0.5	0.9810	0.2410	0.8690	0.9744	0.2385	0.8546
	0.8	0.9915	0.0385	0.3590	0.9838	0.0340	0.3542
10	0.2	0.9753	0.5073	1.3152	0.9673	0.4853	1.2992
	0.5	0.9818	0.2387	0.8781	0.9747	0.2395	0.8579
	0.8	0.9960	0.0394	0.3620	0.9836	0.0357	0.3587
15	0.2	0.9752	0.5074	1.3154	0.9674	0.4856	1.2992
	0.5	0.9818	0.2385	0.8782	0.9747	0.2399	0.8579
	0.8	0.9967	0.0394	0.3625	0.9838	0.0358	0.3586

5.1. Model validation and convergence analysis

It is important to note that for $Gh = 0$, the present model reduces to the model of Evans and Porter (1995). To validate our present theory, we compare the total efficiency η against Kh over the rigid bed with the result obtained by Evans and Porter (1995) in the case of a single-chambered OWC device over a rigid bottom. The results from Evans and Porter (1995) are depicted by the black solid line, while the outcomes of the present study are represented by red squares in Fig. 4(a). It is evident that the present theory aligns well with the results obtained in Ref. Evans and Porter (1995).

Moreover, the present results are also validated with the experimental outcomes reported by Ning et al. (2016) in Fig. 4(b). The solid black line in the figure represents the present theory, while the star points depict the experimental data from Ning et al. (2016). It is noteworthy that in the research conducted by Ning et al. (2016), there is a consideration of the width of the barrier. In contrast, the present study does not account for the width of the barrier, leading to a slight deviation in the validation with the present results, as depicted in Fig. 4(b).

Prior to conducting the numerical calculations, a convergence analysis has been executed for both BEM and EEM. Table 2 shows that the efficiency of OWC, radiation susceptance, and radiation conductance obtained by both EEM and BEM for different OWC heights, a/h with fixed values of $L/h = 1$, $\theta = 20°$, $k_0h = 1.2$ and $Gh = 0.8$. It is noted that the numerical solutions closely align with the analytical solutions. Table 2 demonstrates that ensuring convergence for both EEM and BEM necessitates approximately $10-15$ evanescent modes. Consequently, for the subsequent results in this study, the number of evanescent modes, denoted as $N = 10$, is utilized.

5.2. Efficiency of an OWC with real state data

In this subsection, some seasonal real-state data of an installed OWC at the coast of Tramandai Beach in south Brazil (Strauch et al., 2009; D'Aquino et al., 2019) have been used in the present physical model to examine the efficiency of an OWC over a rigid bottom ($Gh = 0$) and flat porous bottom ($Gh \neq 0$) as depicted in Table 3. This table outlines various parameters, namely T, H, and λ_0 representing the time period, incident wave height, and wavelength, respectively. These wave parameters are categorized according to different seasons, including spring, summer, fall, winter, and annually. The efficiency of OWC has been calculated using both EEM and BEM for a fixed water depth, $h = 17$ m, and OWC width, $L = 0.79$ m with all seasonal data (Strauch

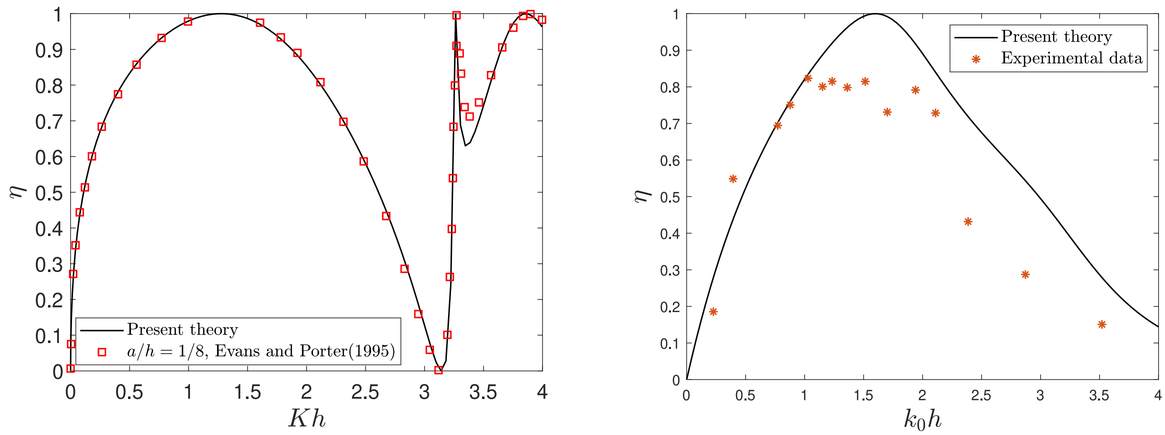

(a) (b)

Fig. 4. (a) Comparison of the present study with (a) the theoretical result obtained by Evans and Porter (1995) for $a/h = 1/8$, $h = 4$m, $L/h = 1$ and (b) the experimental result obtained by Ning et al. (2016) for $h = 0.8$m, $a/h = 0.19$, $L/h = 0.7$ while keeping the fixed value of the porosity parameter $Gh = 0$ and the incident angle $\theta = 0°$.

Table 3
The efficiency based on seasonal wave parameters (Strauch et al., 2009; D'Aquino et al., 2019) using both EEM and BEM for both rigid and porous bottoms.

Season	Wave parameters			η $(Gh = 0)$		η $(Gh = 0.8)$		η $(Gh = 2.5)$	
	T (s)	H (m)	λ_0 (m)	EEM	BEM	EEM	BEM	EEM	BEM
Spring	6.66	1.22	64.28	0.1871	0.1865	0.1704	0.1699	0.1945	0.1941
Summer	7.17	1.33	72.15	0.1618	0.1603	0.1457	0.1417	0.1819	0.1805
Fall	7.86	1.15	82.38	0.1379	0.1372	0.1230	0.1219	0.1650	0.1634
Winter	7.79	1.36	81.46	0.1398	0.1384	0.1247	0.1243	0.1664	0.1658
Annual	7.66	1.23	79.47	0.1439	0.1427	0.1286	0.1277	0.1697	0.1693

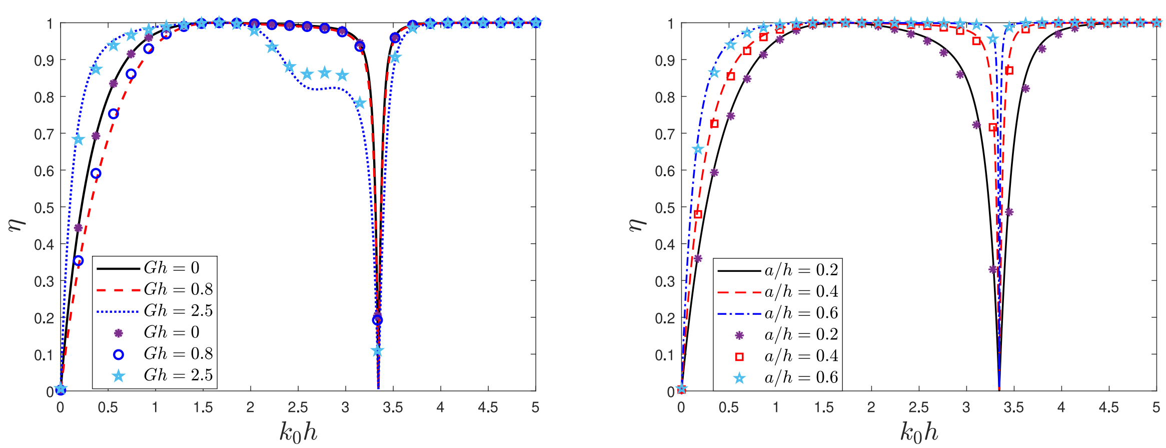

(a) (b)

Fig. 5. Plot depicting the maximum efficiency of OWC (η) as a function of dimensionless wavenumber (k_0h) under different conditions: (a) for various porosity parameters Gh with $a/h = 0.4$ and (b) for different heights of the barrier (a/h) with $Gh = 0.8$. The symbols depict the results obtained by the BEM while each line shows the results obtained by the EEM.

et al., 2009; D'Aquino et al., 2019). The other fixed parameters such as the oblique incident wave angle, $\theta = 20°$ and barrier height, $a/h = 1/8$. From this table, it is found that the results obtained by both EEM and BEM are matched well. Notably, the OWC device exhibits a comparable efficiency over a porous bed ($Gh \neq 0$) as it does over a rigid bed ($Gh = 0$). Thus, Table 3 confirms that the performance of the OWC remains robust even in the presence of a flat porous bed.

5.3. Impacts of different wave and structural factors

Fig. 5 portrays the plot between the maximum efficiency (η) of OWC and dimensionless wavenumber k_0h for different values of the (a) porosity Gh with $a/h = 0.4$ and (b) barrier length a/h with $Gh = 0.8$. From Fig. 5(a), it is observed that full efficiency occurs for $1 < k_0h < 2.5$ for a smaller range of Gh; however, due to more dissipation of energy by the porous bed for larger Gh, full efficiency does not occur in the whole range of $1 < k_0h < 2.5$. On the other hand, zero efficiency occurs when $k_0h = 3.4$ for all the parameters. This phenomenon occurs due to increased OWC length, the movements of fluid like a sloshing mode, resembling the behavior as if it is inside a closed tank with parallel sides. It can be easily seen that in a closed tank, the sloshing frequency occurs at the dimensionless wavenumber $k_0L = n\pi$ as discussed in Evans and Porter (1995). Thus, in this case, the sloshing mode occurs at $k_0h = 3.4$ for fixed OWC width,

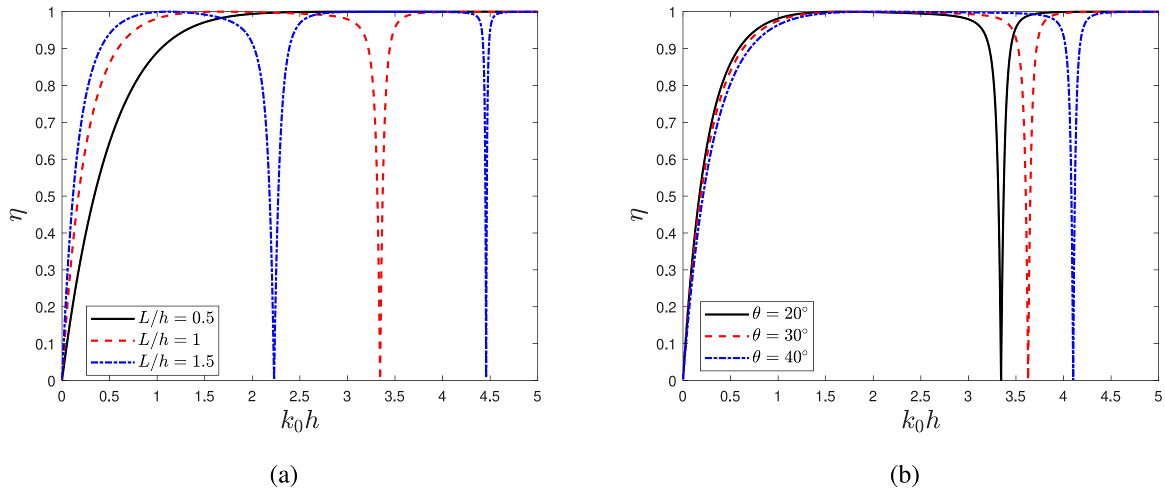

Fig. 6. Plot depicting the maximum efficiency of OWC (η) versus dimensionless wavenumber (k_0h) under different conditions: (a) for various OWC widths (L/h) with $\theta = 20°$, and (b) for different incident angles (θ) with $L/h = 1$. The remaining parameters are held constant at $Gh = 0.8$ and $a/h = 0.4$.

$L/h = 1$. The full efficiency is obtained for $k_0h > 3.4$. It is worth noting that the variation of the efficiency due to the different values of the porous effect parameter Gh is not uniform. Moreover, although the wave energy dissipates by the porous bottom, the full efficiency is observed for specific and OWC wave parameters as observed in the case of the rigid bottom.

Fig. 5(b) reveals that the efficiency increases with an increase in the barrier height a/h. The reason for the phenomenon is that the maximum amount of power absorption in the chamber can be obtained when the resonance frequency of the water column inside the OWC system is the same as the frequency of the incoming waves. In addition, it is anticipated that as the barrier length increases, more water particles will travel a longer distance inside the OWC chamber during one oscillation cycle. As a result, the efficiency of the device increases significantly. Furthermore, the motion of the water column inside the OWC device is assumed to be resonant piston-like motion (Rezanejad et al., 2013). OWC devices should include this feature since it makes the conversion of wave energy to electrical energy more effective. Moreover, the range of k_0h for full efficiency increases for increasing the values of barrier height. Both the figures conclude that full efficiency can be found in the presence of a porous sea bed and also, it is evident that the numerical results matched well with the analytical results. To avoid the time consumption for BEM, analytical results are plotted to examine the effects of wave and structural parameters for an effective OWC in the subsequent results.

The effects of OWC width L/h and incident angle θ on the efficiency of OWC are analyzed in Fig. 6(a) and (b), respectively. Fig. 6(a) shows that the efficiency exponentially increases in a smaller range of k_0h then attains full efficiency. The maxima of efficiency are observed for smaller values of k_0h for increasing the chamber width. The increased size of the air chamber, capable of storing greater amounts of air and generating more power plays a key role in enhancing efficiency. Moreover, in a certain range of k_0h ($0 < k_0h < 5$), zero efficiency does not occur for a smaller chamber width; however, more than one time nearly zero efficiency is observed. This phenomenon occurs because when the incoming wave collides with a solid wall and a barrier within the chamber, it exhibits a motion similar to that of a piston inside the chamber after which as the width of OWC increases then the typical water particle has to cover a greater distance inside the chamber during one oscillation. In that scenario, the widened chamber induces a more intricate pattern of oscillations that leads the deviation in the efficiency. That is why, more zero efficiencies are observed inside the chamber as already discussed in Rezanejad et al. (2013).

In Fig. 6(b), the full efficiency shifts to the right for increasing the angle of the incident wave as k_0h increases more. Zero efficiency is observed for larger values of k_0h. It can be also seen that there is a right shifting in the zero efficiency for a larger angle of the incident wave which may happen due to the first resonance mechanism.

Fig. 7 displays the effectiveness of the radiation susceptance against various (a) porosity parameters and (b) barrier height. In Fig. 7(a), for a non-porous sea bed ($Gh = 0$), in the long wave region, the maxima of the radiation susceptance is observed at nearly $k_0h = 0.5$. There is a significant decrease in the radiation susceptance as Gh increases. Moreover, the maxima and minima of the radiation susceptance curve are found. It is evident from Fig. 7(b) that an oscillating pattern is observed in the curve of radiation susceptance. It is also seen that the radiation susceptance curve first increases as k_0h increases but after attaining maxima, the radiation susceptance decreases for the long-wave region. The initial peak in the radiation susceptance curve happens in the long wave regime due to the first resonance mechanism. In region $0 < k_0h < 1.6$, the radiation susceptance decreases for an increased barrier height.

To analyze the effect of the radiation susceptance against k_0h for different OWC widths and incident angles, Fig. 8 is illustrated. Fig. 8(a) delineates that for a smaller value of OWC width, the radiation susceptance increases as k_0h increases, but after reaching its maxima, it decreases as k_0h further increases. According to Eq. (37), there exists a direct correlation between radiation susceptance and chamber width, denoted as $\mu \propto 1/L$. This signifies that as the chamber width (L) increases, the radiation susceptance undergoes a proportional decrease. This relationship is visually confirmed through the observations presented in Fig. 8(a). Also, if $L \to \infty$ then radiation susceptance, $\mu \to 0$.

Furthermore, for a smaller OWC width, there is no oscillation pattern, whereas when the OWC width is increased, the occurrence of oscillation patterns becomes more in comparison to Fig. 7(a). The amplitude of the oscillatory pattern of the curve decreases for increasing k_0h. This is because the distance that the water particle travels during one oscillation increases with an increase in OWC chamber width. In Fig. 8(b), as incident angle θ increases, a noticeable reduction is observed in the radiation susceptance. For a smaller angle, the radiation susceptance initially increases in $0 < k_0h < 0.7$ and decreases in the region $0.7 < k_0h < 3.4$. It is also seen that for a larger incident angle, the radiation susceptance shifts to the right side for $k_0h > 3.4$. Also, the maxima and minima of the radiation susceptance are found for all incident angles θ.

The behavior of radiation conductance (ν) of OWC against the dimensionless wavenumber (k_0h) has been shown for different values of (a) porosity parameter Gh (b) barrier height a/h in Fig. 9. The radiation conductance decreases as the porosity parameter increases due to the

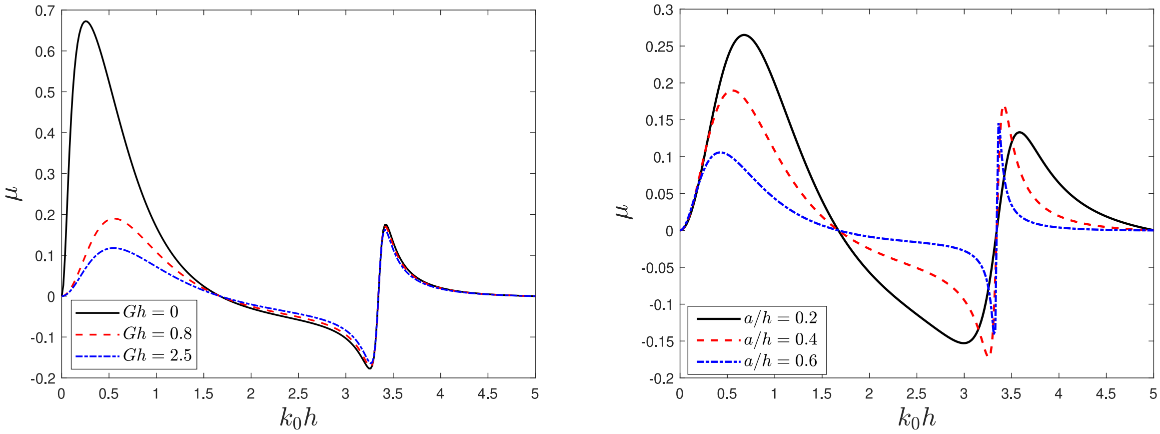

(a) (b)

Fig. 7. Plot depicting the radiation susceptance of OWC (μ) as a function of the dimensionless wavenumber (k_0h) under different conditions: (a) for different porosity parameters Gh with $a/h = 0.4$ and (b) for various barrier heights (a/h) with $Gh = 0.8$. The remaining parameters are held constant at $\theta = 20°$ and $L/h = 1$.

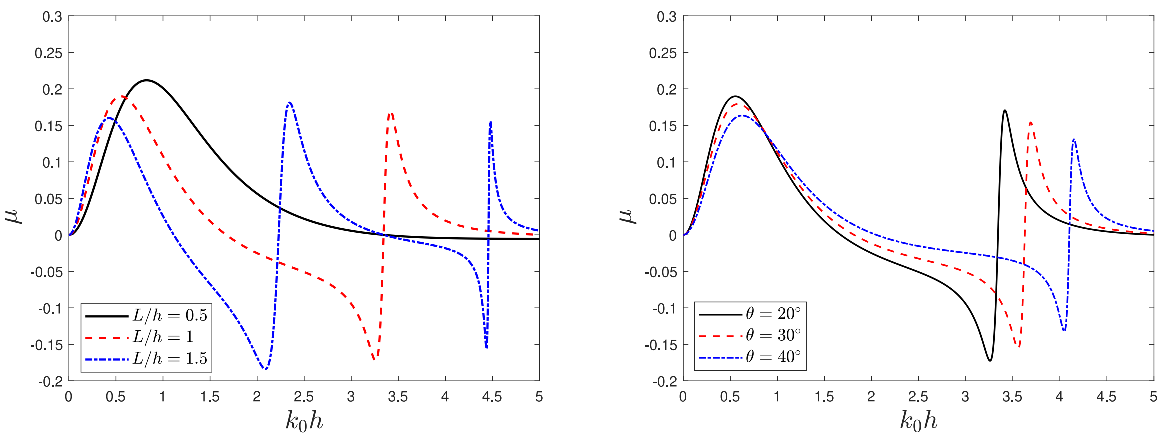

(a) (b)

Fig. 8. Plot depicting the radiation susceptance of OWC (μ) versus the dimensionless wavenumber (k_0h) under different conditions: (a) for various OWC widths (L/h) with $\theta = 20°$ and (b) for different incident angles (θ) with $L/h = 1$. The remaining parameters are held constant at $a/h = 0.4$ and $Gh = 0.8$.

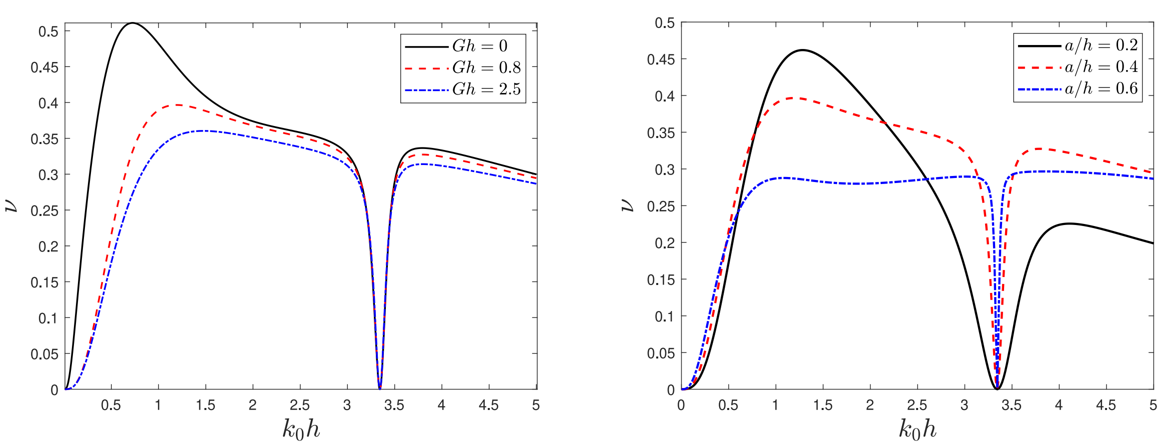

(a) (b)

Fig. 9. Plot depicting the radiation conductance of OWC (ν) as a function of dimensionless wavenumber (k_0h) under different conditions: (a) for various porosity parameters (Gh) with $a/h = 0.4$, and (b) for different barrier heights (a/h) with $Gh = 0.8$. The remaining parameters are held constant at $\theta = 20°$ and $L/h = 1$.

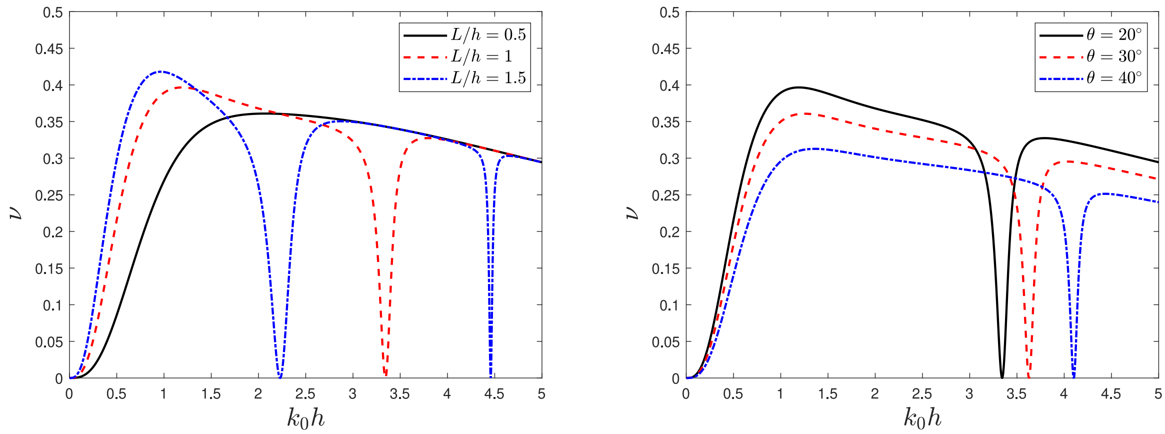

(a) (b)

Fig. 10. Plot depicting the radiation conductance (ν) of OWC as a function of dimensionless wavenumber (k_0h) under different conditions: (a) for various OWC widths (L/h) with $\theta = 20°$, and (b) for different incident angles (θ) with $L/h = 1$. The remaining parameters are held constant at $Gh = 0.8$ and $a/h = 0.4$.

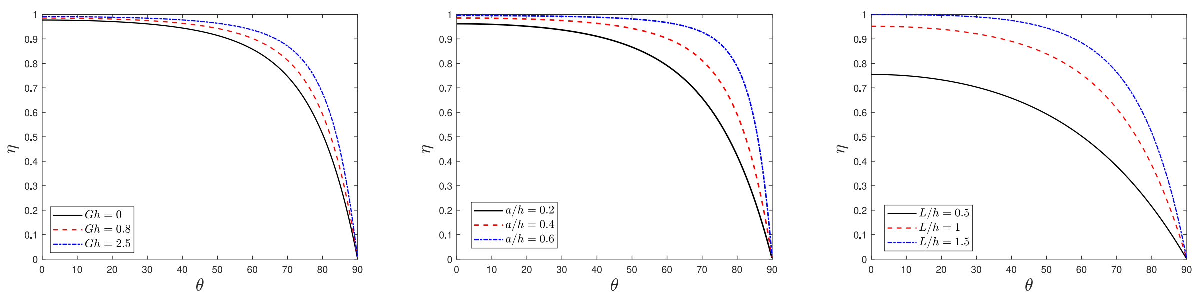

(a) (b) (c)

Fig. 11. Plot illustrating the efficiency of OWC (η) with the incident wave angle (θ) under different conditions: (a) for various porosity parameters Gh with $a/h = 0.4$ and $L/h = 1$, (b) for different barrier heights (a/h) with $Gh = 0.8$ and $L/h = 1$, and (c) for varying OWC widths (L/h) with $Gh = 0.8$ and $a/h = 0.4$.

porosity of the seabed that absorbs some of the wave energy. It is also observed from Fig. 9(a) that zero radiation conductance is found for all values of Gh at $k_0h = 3.4$. Moreover, the radiation conductance curve initially increases within the range of $0 < k_0h < 1$ and subsequently decreases within the range of $1 < k_0h < 3.4$. From Fig. 9(b), it can be noted that when the barrier height is increased, there is a significant reduction in the radiation conductance within a range of $0.5 < k_0h < 2.4$ due to the second resonance mechanism, that is the sloshing effect.

The plot between the radiation conductance against k_0h for various values of OWC width and the incident angle is found in Fig. 10. Fig. 10(a) demonstrates that for a smaller OWC width, the radiation conductance initially increases as k_0h increases, but after a certain value of k_0h, it subsequently diminishes with further increases in k_0h. Additionally, for a smaller OWC width, there is no zero radiation conductance. In contrast, as the OWC width increases, the occurrence of zero radiation conductance is observed more. This may happen due to the first resonance mechanism. It is evident that the zero radiation conductance shifts to the left when the OWC width is greater. In Fig. 10(b), as the angle of incidence increases, the radiation conductance decreases and undergoes a rightward shift when $k_0h > 3.4$. Additionally, it is worth noting that there is consistent growth in the radiation conductance within the range of $0 < k_0h < 3$. Furthermore, it exhibits zero radiation conductance for each angle of incidence.

The effect of the porosity parameter, barrier height, and the OWC width on the efficiency of OWC is delineated in Fig. 11. Fig. 11(a) shows that the efficiency increases as Gh increases and the full efficiency is noticed for a more immense value of the porosity parameter. Moreover, for a larger value of Gh, there is a right shift in the efficiency curve for $\theta > 40°$. In both Fig. 11(b) and (c), as barrier height increases, the nearly full efficiency is observed, similar to Fig. 11(a). This phenomenon occurs due to the interface between the incident and the reflected wave. It is also noticed that the efficiency rapidly approaches a value of 1 for larger values of the parameters Gh, a/h, and L/h, indicating full efficiency in Fig. 11. This is accurate since an incident wave that is almost totally transmitted inside the long-wave limit cannot be experienced in the OWC chamber.

The importance of the porosity parameter, barrier height, and OWC width on the radiation conductance against the angle of incidence is depicted in Fig. 12. In Fig. 12(a), as the porosity parameter increases the radiation conductance (η) decreases within the range of $0° < \theta < 60°$ due to the porous bed. Fig. 12(b) shows that within a specific range of incident angle, $0° < \theta < 40°$, the radiation conductance diminishes as the barrier length increases. Moreover, the radiation conductance nearly approaches zero for $\theta > 80°$. In contrast to Fig. 12(b), the radiation conductance increases for increasing the value of OWC width in Fig. 12(c). A similar observation of zero radiation conductance is found for $\theta > 80°$ in all Fig. 12(a)–(c).

The performance of radiation susceptance with respect to the incident angle is illustrated in Fig. 13 for different values of (a) porosity parameter (b) barrier height and (c) OWC width. From Fig. 13(a) it can be seen that the radiation susceptance of OWC (μ) decreases as Gh increases within the range for $\theta < 70°$. For a larger value of Gh, there is minimal change in the radiation susceptance curve for $\theta = 70°$. In Fig. 13(b), for larger barrier height, there is a significant reduction in the radiation susceptance. Furthermore, when the barrier height is lower, we observe nearly constant radiation susceptance within the range of $0° < \theta < 40°$ while for the larger barrier height, the range of incident angle is increased where the radiation susceptance is

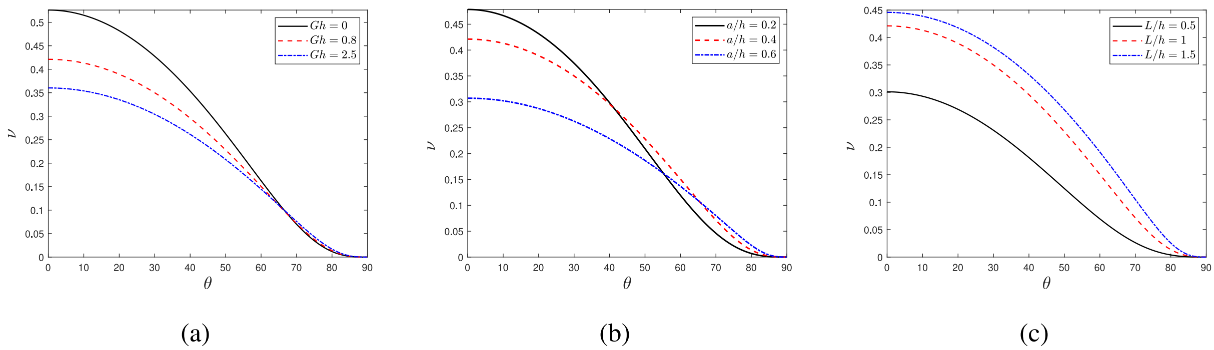

Fig. 12. Plot illustrating the variation of the radiation conductance (ν) of OWC with the incident wave angle (θ) under different conditions: (a) for various porosity parameters Gh with $a/h = 0.4$ and $L/h = 1$, (b) for different barrier heights (a/h) with $Gh = 0.8$ and $L/h = 1$, and (c) for varying OWC widths (L/h) with $Gh = 0.8$ and $a/h = 0.4$.

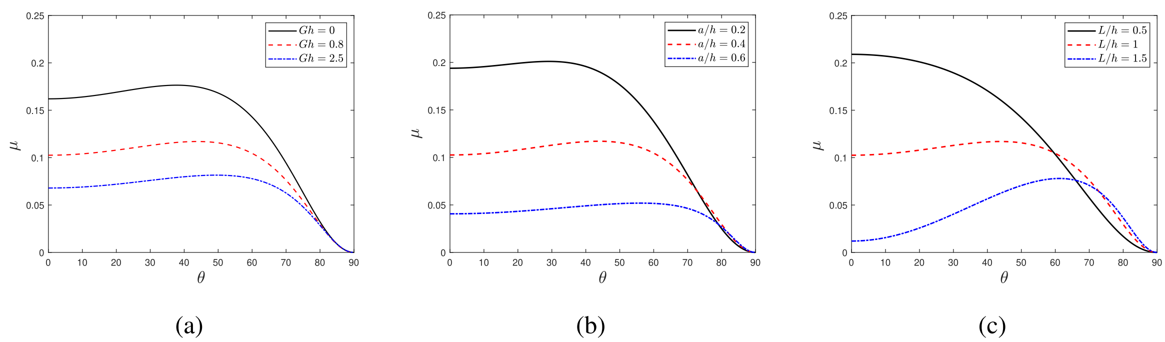

Fig. 13. Plot illustrating the variation of the radiation susceptance (μ) of OWC with the incident wave angle (θ) under different conditions: (a) for various porosity parameters Gh with $a/h = 0.4$ and $L/h = 1$, (b) for different barrier heights (a/h) with $Gh = 0.8$ and $L/h = 1$, and (c) for varying OWC widths (L/h) with $Gh = 0.8$ and $a/h = 0.4$.

nearly constant. Fig. 13(c) illustrates that with a smaller OWC width, the radiation susceptance consistently decreases as the incident angle increases. However, with a larger OWC width, there is a slight increase in radiation susceptance, and beyond $\theta > 60°$, it begins to decrease. In all Fig. 13(a)–(c), the zero radiation conductance is found at $\theta = 90°$.

The variation of efficiency (η) versus dimensionless wavenumber (k_0h) and the incident angle (θ) is plotted in Fig. 14. The minima of the efficiency is observed at $k_0h = 3.2$ in all the Fig. 14(a)–(d). It is also noticeable that as the porosity parameter for $Gh > 0.8$, the full efficiency is observed in a wider range. The energy of waves as they pass through the porous seabed interacts with OWC leading to a resonant effect that amplifies the amount of wave energy captured and utilized by the OWC device. This phenomenon can create patterns of both constructive and destructive interference, causing the efficiency of the system to vary depending on the incident wave angle. The analogous results are also depicted in Fig. 5(a) and Fig. 11(a), where the efficiency (η) is plotted with respect to two variables: the dimensionless wavenumber k_0h and the incident angle θ, respectively.

Fig. 15 displays a surface plot of efficiency η as a function of k_0h and θ for various barrier height (a/h). Fig. 15(a) clearly illustrates that maximum efficiency is noticed within two specific ranges: $0.7 < k_0h < 3.4$ and $3.4 < k_0h < 5$. This occurs because when the water is stirred up by the incoming wave, it causes movements inside the OWC chamber, like piston motion. Furthermore, both Fig. 15(a) and (b) reveal that efficiency drops to zero at a specific value of $k_0h = 3.2$. The comparison demonstrates that as the barrier height increases, there is a greater enhancement in energy conversion efficiency. Moreover, an optimal selection of the barrier height a/h and the incident angle θ leads to an augmentation in the efficiency of the OWC device. A similar outcome is also illustrated in Figs. 5(b) and 11(b), where efficiency (η) is presented as a function of k_0h and θ, respectively.

Fig. 16 portrays how the efficiency (η) varies with the dimensionless wavenumber (k_0h) and the angle (θ), considering different values of OWC width (L/h). In Fig. 16(a), it is clear that the efficiency curve does not exhibit any oscillation. This occurs when the chamber width of the OWC is smaller, it enables more effective energy transportation between the incoming wave and the OWC device. Conversely, in Fig. 16(b), as the OWC width increases, we observe minima in the efficiency curve. This is because a wider chamber can potentially lead to less effective energy transportation between the incoming wave and the OWC device. Therefore, an optimal value of the OWC width is crucial to optimize the efficiency of the OWC device. There is a similar depictions in Figs. 6(a) and 11(c) for the efficiency against k_0h and θ, respectively.

Fig. 17 presents a surface plot showcasing the variation of radiation susceptance (μ) against both the dimensionless wavenumber (k_0h) and the incident angle (θ). In this plot, the radiation susceptance exhibits its highest peak within the long wave region whereas its trough is within the short wave region. In both Fig. 17(a) and (b), it is evident that as the porosity parameter Gh increases, the curve representing radiation susceptance shows a more significant decrease. This occurs because the porous bed absorbs some of the portion of the wave energy, and it might also be attributed to the presence of multiple resonances within the OWC system. The outcomes observed in Figs. 7(a) and 13(a) exhibit a resemblance to the illustration in Fig. 17.

Fig. 18 examines the impact of radiation susceptance against the wavenumber (k_0h) and incident angle (θ) through a surface plot. In Fig. 18(a), the radiation susceptance curve exhibits an initial rise within a smaller range of wavenumber. However, as the wavenumber continues to increase, a reduction in the radiation susceptance becomes evident. This occurs because when the wavenumber is high, the wavelength of the wave becomes smaller than the size of the OWC device. In such cases, the device cannot efficiently capture energy from the wave. In Fig. 18(b), for larger barrier height, the radiation susceptance reduces more in comparison to Fig. 18(b). Similar results are presented in Figs. 7(b) and 13(b) where the radiation susceptance is graphed in relation to both the frequency represented as k_0h and the incident angle θ.

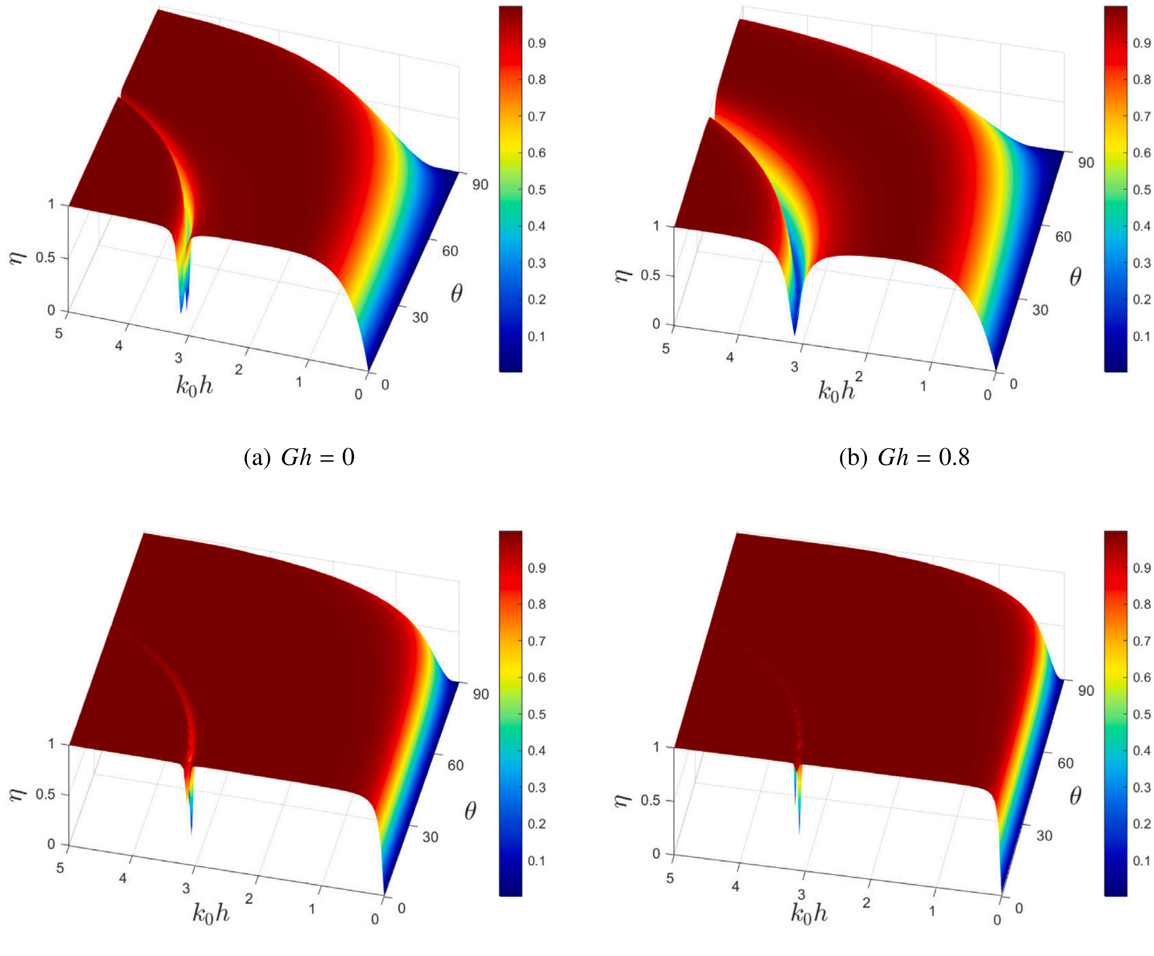

(a) $Gh = 0$ (b) $Gh = 0.8$

(c) $Gh = 1.5$ (d) $Gh = 2.5$

Fig. 14. Surface representation depicting the efficiency of OWC against the dimensionless wavenumber (k_0h) and the angle of incidence (θ) for the different porosity parameters Gh. The remaining parameters are held constant at $a/h = 0.4$ and $L/h = 1$.

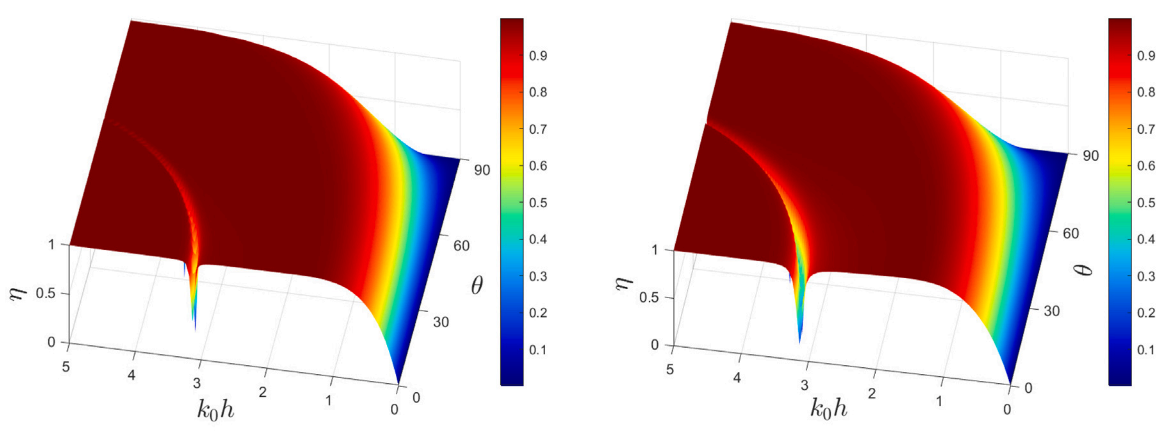

(a) $a/h = 0.4$ (b) $a/h = 0.6$

Fig. 15. Surface representation depicting the efficiency of OWC against the dimensionless wavenumber (k_0h) and the angle of incidence (θ) for various heights of the barrier (a/h). The remaining parameters are held constant at $Gh = 0.8$ and $L/h = 1$.

To understand how the radiation susceptance (μ) behaves against the wavenumber k_0h and the incident angle θ for various OWC widths, a surface plot is presented in Fig. 19. In Fig. 19(a), within the long wave region, the radiation susceptance rises as the frequency increases. However, after reaching its peak, the radiation susceptance decreases for $k_0h > 1.7$. Fig. 19(b) illustrates that when the width of the OWC is enlarged, we observe a greater number of peaks and troughs in the radiation susceptance curve. Additionally, it demonstrates that as the wavenumber increases, the susceptance curve decreases. This can be attributed to the same explanation provided in Fig. 18. Furthermore,

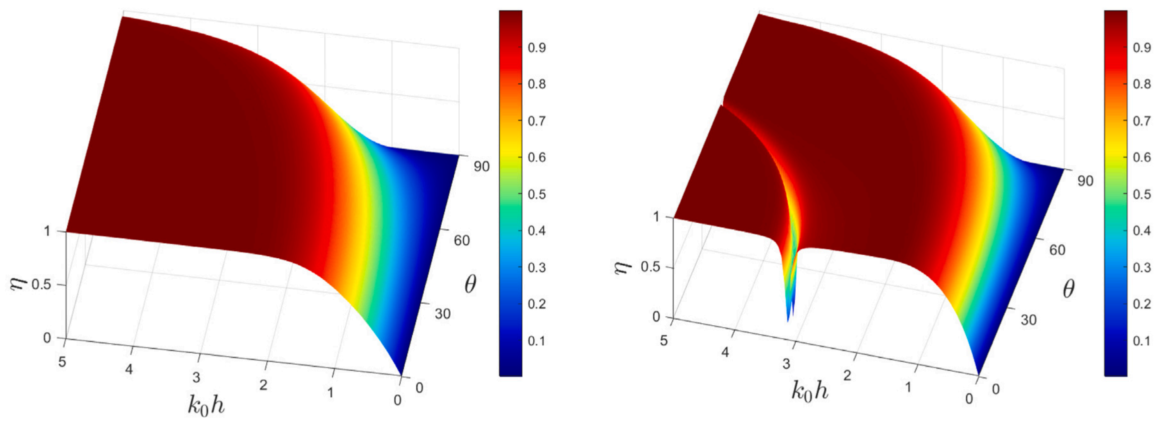

(a) $L/h = 0.5$ (b) $L/h = 1$

Fig. 16. Surface representation depicting the efficiency (η) of the OWC as a function of the dimensionless wavenumber (k_0h) and the incident wave angle (θ), with varying OWC widths L/h. The remaining parameters are held constant at $Gh = 0.8$ and $a/h = 0.4$.

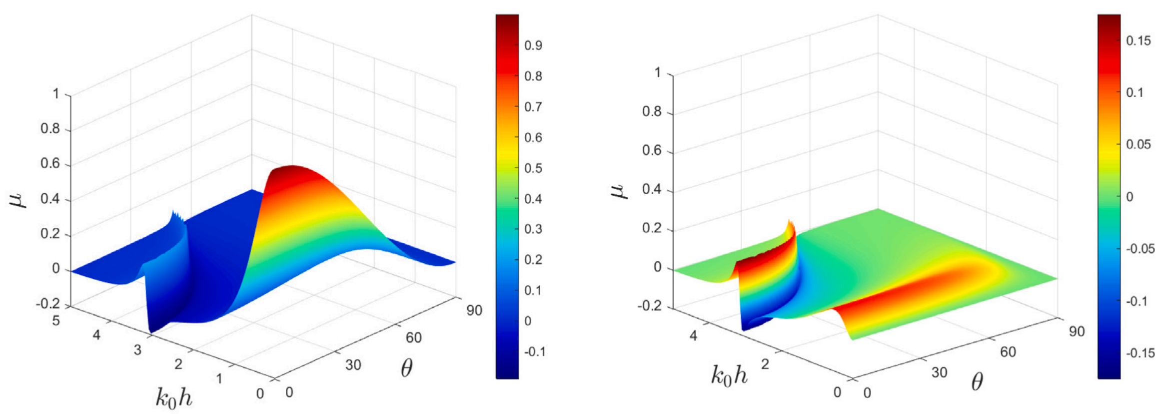

(a) $Gh = 0$ (b) $Gh = 2.5$

Fig. 17. Surface representation depicting the radiation susceptance (μ) of OWC against non-dimensional wavenumber (k_0h) and incident wave angle (θ) for different porosity parameters Gh. The remaining parameters are held constant at $a/h = 0.4$ and $L/h = 1$.

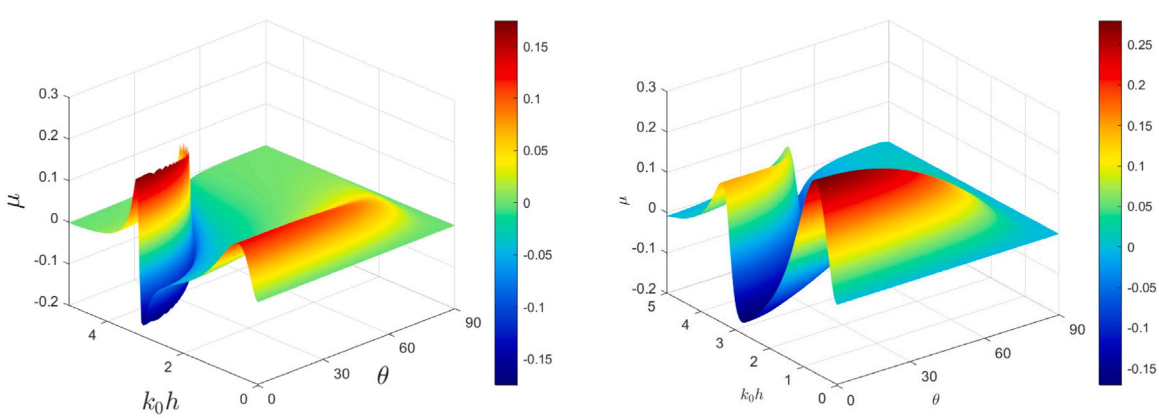

(a) $a/h = 0.4$ (b) $a/h = 0.6$

Fig. 18. Surface representation depicting the radiation susceptance (μ) of OWC as a function of the dimensionless wavenumber (k_0h) and angle of the incident wave (θ) for various barrier height (a/h). The remaining parameters are held constant at $Gh = 0.8$ and $L/h = 1$.

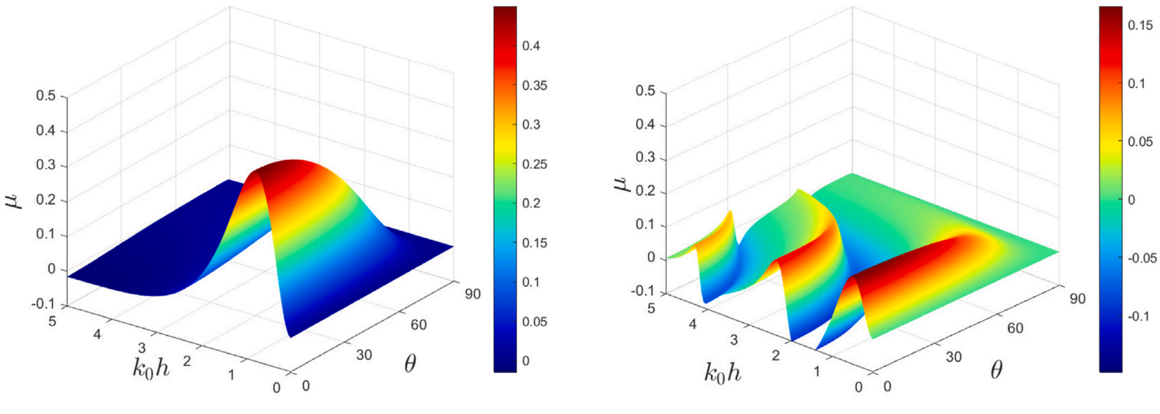

(a) $L/h = 0.5$ (b) $L/h = 1.5$

Fig. 19. Surface representation depicting the radiation susceptance of OWC (ν) as a function of the dimensionless wavenumber (k_0h) and angle of the incident wave (θ) for various barrier height. The remaining parameters are held constant at $a/h = 0.4$ and $Gh = 0.8$.

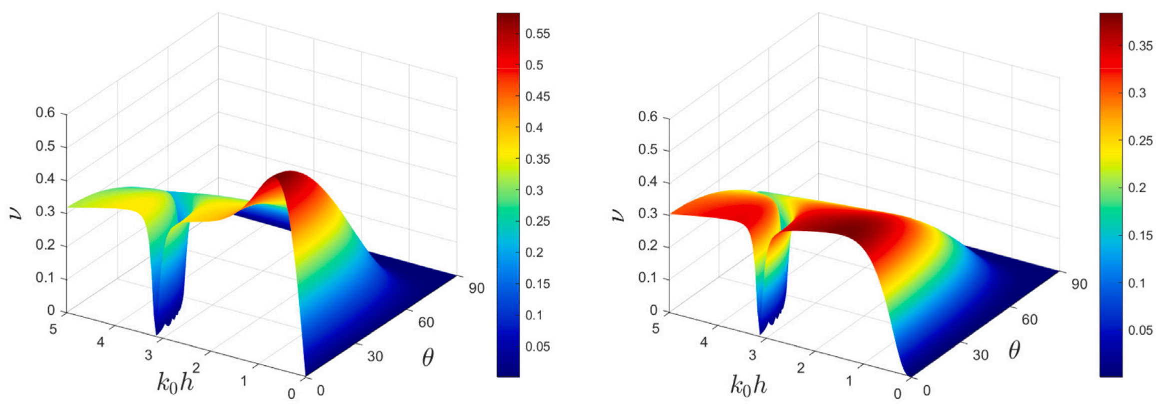

(a) $Gh = 0$ (b) $Gh = 2.5$

Fig. 20. Surface representation depicting the radiation conductance of OWC (ν) as a function of the dimensionless wavenumber (k_0h) and angle of incident wave (θ) for different porosity parameters Gh. The remaining parameters are held constant at $a/h = 0.4$ and $L/h = 1$.

the outcomes in Figs. 8(a) and 13(c) exhibit analogous patterns to the results observed in Fig. 19.

The variation of the radiation conduction ν as a function of wavenumber and incident angle for different values of Gh is plotted in Fig. 20. In Fig. 20(a), it is evident that the radiation conductance is higher compared to Fig. 20(b) due to the larger values of the porosity parameter. In both Fig. 20(a) and (b), the maxima and minima occur in the radiation conductance curve also the minima is noted as $k_0h = 3.2$. The behavior of the radiation conductance in Fig. 20 is observed similar to the results presented in Figs. 9(a) and 12(a).

Fig. 21 illustrates the effect of the radiation conductance in the function of (k_0h, θ) for different values of barrier height (a/h). From both Fig. 21(a) and (b), it is evident that initially, for lower wavenumber, the conductance tends to rise, indicating improved energy transmission through the barrier. However, as the wavenumber increases further, the conductance begins to decrease. This happens because, at high wavenumber, the wavelength of the wave becomes shorter than the size of the OWC device. The minima in the conductance curve are observed at nearly $k_0h = 3.2$. The same effects of the conductance curve are seen in Figs. 9(a) and 12(b).

To visualize the behavior of radiation conduction as a function of (k_0h, θ), a surface plot is presented for various OWC width values. Fig. 22(a) shows that smaller OWC widths do not exhibit zero radiation conductance, whereas larger OWC widths reveal multiple instances of zero radiation conductance as shown in Fig. 22(b). Also, it is noticed that there is a greater reduction in the radiation conductance for a larger value of OWC width. The analogous results of the conductance are noticed in Figs. 10(a) and 12(c).

6. Conclusion

This paper examines the efficiency of a single-chambered OWC device near a rigid wall over a porous bed under the assumption of the linearized water wave theory and the small amplitude of the surface waves. The associated boundary value problem is tackled using both analytical and numerical techniques via the EEM and BEM, respectively. The comparison of the analytical and numerical results reveals a good agreement. The present study shows that the porous bed has a notable impact on the characteristics of the OWC device.

Furthermore, in the long wave region, the efficiency curve in relation to wavenumber initially increases before reaching its maximum efficiency. However, because of dissipation caused by the porous bed, the maximum efficiency is not obtained throughout the entire range of $0 < k_0h < 2.5$ when the porosity parameter is higher. Moreover, the maximum efficiency is observed against wavenumber for higher values of OWC chamber width in the long wave region. The larger dimensions of the air chamber, enabling it to store larger quantities of air and produce more power, are crucial for improving efficiency.

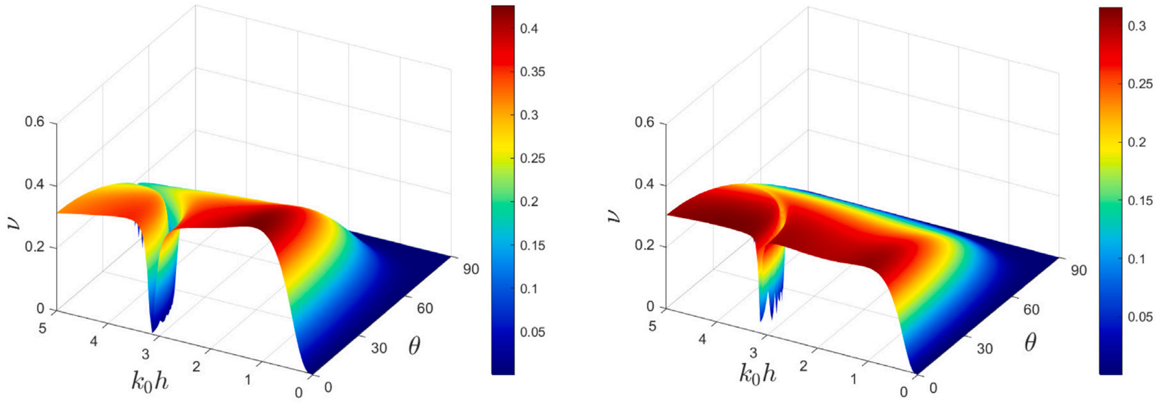

(a) $a/h = 0.4$ (b) $a/h = 0.6$

Fig. 21. Surface representation depicting the radiation conductance of OWC (ν) as a function of the dimensionless wavenumber (k_0h) and angle of incident wave (θ) for various barrier height. The remaining parameters are held constant at $Gh = 0.8$ and $L/h = 1$.

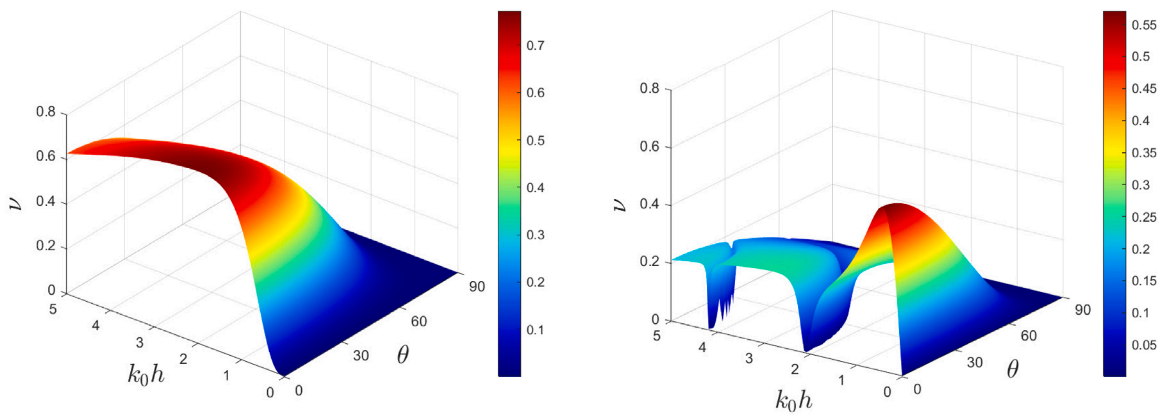

(a) $L/h = 0.5$ (b) $L/h = 1.5$

Fig. 22. Surface representation depicting the radiation conductance of OWC (ν) as a function of the dimensionless wavenumber (k_0h) and angle of incident wave (θ) for various OWC widths. The remaining parameters are held constant at $Gh = 0.8$ and $a/h = 0.4$.

The efficiency of the OWC device with respect to the incident angle, is observed that with an increase in porosity of the bottom, barrier height, and OWC width, the full efficiency is found within the range of the incident angle $0° < \theta < 30°$. Moreover, the efficiency of OWC against incident angle increases as the height of the barrier increases, and with increasing value of the porosity parameter, the efficiency curve decreases. On the other hand, the radiation conductance and radiation susceptance with respect to the incident angle θ decrease when the height of the barrier increases. Additionally, an increase in the width of the OWC leads to an increase in radiation conductance and a reduction in radiation susceptance. Also, the oscillation pattern is observed while plotting the radiation susceptance as a function of two parameters: the dimensionless wavenumber (k_0h) and incident angle θ for a wider value of OWC width.

Overall, a single-chambered OWC device near a wall over a porous bed consistently exhibits the significant amount of the efficiency, underscoring its potential for enhancing the performance of the device.

CRediT authorship contribution statement

Nikita Naik: Writing – original draft, Validation, Methodology, Investigation, Formal analysis. **Aman Kumar Kushwaha:** Writing – original draft, Validation, Methodology, Investigation, Formal analysis. **Harekrushna Behera:** Writing – review & editing, Validation, Supervision, Software, Methodology, Investigation, Formal analysis, Conceptualization. **Chia-Cheng Tsai:** Writing – review & editing, Investigation, Funding acquisition.

Declaration of competing interest

The authors declare the following financial interests/personal relationships which may be considered as potential competing interests: Harekrushna Behera reports financial support was provided by Science and Engineering Research Board, India and the National Science and Technology Council, Taiwan. Harekrushna Behera reports a relationship with Science and Engineering Research Board that includes: funding grants. Harekrushna Behera has patent pending to NA. The authors declare that they have no known competing financial interests or personal relationships that could have appeared to influence the work reported in this paper.

Data availability

No data was used for the research described in the article.

Acknowledgments

H.B. gratefully acknowledges the financial support from the Science and Engineering Research Board, Dept. of Science and Technology, Govt. of India, through the MATRICS project (Award Number MTR/2021/000870). H.B. acknowledges the financial support from the National Science and Technology Council of Taiwan (Grant No. NSTC 112-2811-E-019-003). C-C.T. acknowledges the financial support from the National Science and Technology Council of Taiwan (Grant No. NSTC 112-2221-E-019-050-MY3).

Appendix

Nomenclature

η	Efficiency of the OWC device
Λ	Positive real constant
λ	Euler's constant
λ_0	Wave length
$\mathcal{G}$	Green's function
$\mathscr{E}_W$	Total wave energy per wave period
μ	Dimensionless radiation susceptance
ν	Dimensionless radiation conductance
ω	Angular frequency
Φ	Velocity potential
ϕ	Spatial velocity potential
$\mathfrak{R}$	Real part of the complex number
ρ	Density of the water
θ	Incident wave angle
$\tilde{\alpha}$	Radiation conductance
$\tilde{\beta}$	Radiation susceptance
$\tilde{\mathfrak{I}}$	Imaginary part of the complex number
a	Height of the thin barrier
c_g	Group velocity
G	Porous effect parameter
g	Acceleration due to gravity
H	Incident wave height
h	Water depth
I_0	Incident wave amplitude
k_0	Progressive wave number of the incident wave
L	OWC chamber width
p	Pressure inside the OWC chamber
q	Volume flux across the internal free surface
T	Time period
t	Time
W	Average rate of work over a single wave period

References

Babarit, A., Guglielmi, M., Clément, A.H., 2009. Declutching control of a wave energy converter. Ocean Eng. 36, 1015–1024. http://dx.doi.org/10.1016/j.oceaneng.2009.05.006.

Barman, K.K., Bora, S.N., 2022. Analysis of wave reflection, waveload, and pressure distribution due to a poro-elastic structure in a two-layer fluid over a porous sea-bed. J. Ocean Eng. Mar. Energy 8, 331–354. http://dx.doi.org/10.1007/s40722-022-00235-0.

Behera, H., Ng, C.O., Sahoo, T., 2018. Oblique wave scattering by a floating elastic plate over a porous bed in single and two-layer fluid systems. Ocean Eng. 159, 280–294. http://dx.doi.org/10.1016/j.oceaneng.2018.04.031.

Boyle, R., 2008. Global Trends in Sustainable Energy Investment 2008: Analysis of Trends and Issues in the Financing of Renewable Energy and Energy Efficiency.

Chanda, A., Bora, S.N., 2020. Effect of a porous sea-bed on water wave scattering by two thin vertical submerged porous plates. Eur. J. Mech. B Fluids 84, 250–261. http://dx.doi.org/10.1016/j.euromechflu.2020.06.009.

Chang, J.Y., Tsai, C.C., 2022. Wave forces on a partially reflecting wall by oblique Bragg scattering with porous breakwaters over uneven bottoms. J. Mar. Sci. Eng. 10, 409. http://dx.doi.org/10.3390/jmse10030409.

D'Aquino, C.D.A., Scharlau, C.C., Vecchia, L.C.D., 2019. Evaluation of the energy extraction of a small-scale wave energy converter. Rev. Bras. Recur. Hidr. 24, http://dx.doi.org/10.1590/2318-0331.241920180030.

Delmonte, N., Barater, D., Giuliani, F., Cova, P., Buticchi, G., 2014. Oscillating water column power conversion: A technology review. In: 2014 IEEE Energy Conversion Congress and Exposition. ECCE, pp. 1852–1859. http://dx.doi.org/10.1109/ECCE.2014.6953644.

Deng, Z., Wang, P., Cheng, P., 2021. Hydrodynamic performance of an asymmetry OWC device mounted on a box-type breakwater. Front. Mar. Sci. 8, 677030. http://dx.doi.org/10.3389/fmars.2021.677030.

Deng, Z., Wang, C., Wang, P., Higuera, P., Wang, R., 2019. Hydrodynamic performance of an offshore-stationary OWC device with a horizontal bottom plate: Experimental and numerical study. Energy 187, 115941. http://dx.doi.org/10.1016/j.energy.2019.115941.

Deng, Z., Wang, C., Yao, Y., Higuera, P., 2020a. Numerical simulation of an oscillating water column device installed over a submerged breakwater. J. Mar. Sci. Technol. 25, 258–271. http://dx.doi.org/10.1007/s00773-019-00645-0.

Deng, Z., Wang, L., Zhao, X., Wang, P., 2020b. Wave power extraction by a nearshore oscillating water column converter with a surging lip-wall. Renew. Energy 146, 662–674. http://dx.doi.org/10.1016/j.renene.2019.06.178.

Dong, J., Wang, B., Zhao, X., Liu, H., 2018. Wave forces exerted on a submerged horizontal plate over an uneven bottom. J. Eng. Mech. 144, 04018030. http://dx.doi.org/10.1061/(ASCE)EM.1943-7889.0001447.

Doyle, S., Aggidis, G.A., 2019. Development of multi-oscillating water columns as wave energy converters. Renew. Sustain. Energy Rev. 107, 75–86. http://dx.doi.org/10.1016/j.rser.2019.02.021.

Doyle, S., Aggidis, G.A., 2021. Experimental investigation and performance comparison of a 1 single OWC, array and M-OWC. Renew. Energy 168, 365–374. http://dx.doi.org/10.1016/j.renene.2020.12.032.

Drew, B., Plummer, A.R., Sahinkaya, M.N., 2009. A review of wave energy converter technology. Proc. Inst. Mech. Eng. A 223, 887–902. http://dx.doi.org/10.1243/09576509JPE782.

Elhanafi, A., Kim, C.J., 2018. Experimental and numerical investigation on wave height and power take–off damping effects on the hydrodynamic performance of an offshore–stationary OWC wave energy converter. Renew. Energy 125, 518–528. http://dx.doi.org/10.1016/j.renene.2018.02.131.

Evans, D., Porter, R., 1995. Hydrodynamic characteristics of an oscillating water column device. Appl. Ocean Res. 17, 155–164. http://dx.doi.org/10.1016/0141-1187(95)00008-9.

Gubesch, E., Abdussamie, N., Penesis, I., Chin, C., 2022. Maximising the hydrodynamic performance of offshore oscillating water column wave energy converters. Appl. Energy 308, 118304. http://dx.doi.org/10.1016/j.apenergy.2021.118304.

Haghighi, A.T., Nikseresht, A.H., Hayati, M., 2021. Numerical analysis of hydrodynamic performance of a dual-chamber oscillating water column. Energy 221, 119892. http://dx.doi.org/10.1016/j.energy.2021.120326.

Haikonen, K., Sundberg, J., Leijon, M., 2013. Characteristics of the operational noise from full scale wave energy converters in the Lysekil project: Estimation of potential environmental impacts. Energies 6, 2562–2582. http://dx.doi.org/10.3390/en6052562.

He, F., Zhang, H., Zhao, J., Zheng, S., Iglesias, G., 2019. Hydrodynamic performance of a pile-supported OWC breakwater: An analytical study. Appl. Ocean Res. 88, 326–340. http://dx.doi.org/10.1016/j.apor.2019.03.022.

Khan, M.B., Behera, H., 2021. Impact of sloping porous seabed on the efficiency of an OWC against oblique waves. Renew. Energy 173, 1027–1039. http://dx.doi.org/10.1016/j.renene.2021.04.046.

Kofoed, J.P., Frigaard, P., Friis-Madsen, E., Sørensen, H.C., 2006. Prototype testing of the wave energy converter wave dragon. Renew. Energy 31, 181–189. http://dx.doi.org/10.1016/j.renene.2005.09.005.

Koley, S., Trivedi, K., 2020. Mathematical modeling of oscillating water column wave energy converter devices over the undulated sea bed. Eng. Anal. Bound. Elem. 117, 26–40. http://dx.doi.org/10.1016/j.enganabound.2020.03.017.

Li, Y., Zhao, X., Zou, Q., Geng, J., 2022. Hydrodynamic performance of dual-chamber oscillating water column array under oblique waves. Phys. Fluids 34, 117112. http://dx.doi.org/10.1063/5.0118655.

Luo, Y., Wang, Z., Peng, G., Xiao, Y., Zhai, L., Liu, X., Zhang, Q., 2014. Numerical simulation of a heave-only floating OWC (oscillating water column) device. Energy 76, 799–806. http://dx.doi.org/10.1016/j.energy.2014.08.079.

Maiti, P., Mandal, B.N., 2014. Water wave scattering by an elastic plate floating in an ocean with a porous bed. Appl. Ocean Res. 47, 73–84. http://dx.doi.org/10.1016/j.apor.2014.03.006.

Martha, S., Bora, S., Chakrabarti, A., 2007. Oblique water-wave scattering by small undulation on a porous sea-bed. Appl. Ocean Res. 29, 86–90. http://dx.doi.org/10.1016/j.apor.2007.07.001.

Morris-Thomas, M.T., Irvin, R.J., Thiagarajan, K.P., 2007. An investigation into the hydrodynamic efficiency of an oscillating water column. J. Offshore Mech. Arct. Eng. http://dx.doi.org/10.1115/1.2426992.

Naik, N., Gayathri, R., Behera, H., Tsai, C.C., 2023a. Wave power extraction by a dual OWC chamber over an undulated bottom. Renew. Energy 216, 119026. http://dx.doi.org/10.1016/j.renene.2023.119026.

Naik, N., Zheng, S., Behera, H., 2023b. Role of dual breakwaters and trenches on efficiency of an oscillating water column. Phys. Fluids 35, 047115. http://dx.doi.org/10.1063/5.0146004.

Ning, D.Z., Shi, J., Zou, Q.P., Teng, B., 2015. Investigation of hydrodynamic performance of an OWC (oscillating water column) wave energy device using a fully nonlinear HOBEM (higher-order boundary element method). Energy 83, 177–188. http://dx.doi.org/10.1016/j.energy.2015.02.012.

Ning, D.Z., Wang, R.Q., Zou, Q.P., Teng, B., 2016. An experimental investigation of hydrodynamics of a fixed OWC wave energy converter. Appl. Energy 168, 636–648. http://dx.doi.org/10.1016/j.apenergy.2016.01.107.

Ning, D., Zhou, Y., Zhang, C., 2018. Hydrodynamic modeling of a novel dual-chamber OWC wave energy converter. Appl. Ocean Res. 78, 180–191. http://dx.doi.org/10.1016/j.apor.2018.06.016.

Rezanejad, K., Bhattacharjee, J., Soares, C.G., 2013. Stepped sea bottom effects on the efficiency of nearshore oscillating water column device. Ocean Eng. 70, 25–38. http://dx.doi.org/10.1016/j.oceaneng.2013.05.029.

Rezanejad, K., Bhattacharjee, J., Soares, C.G., 2015. Analytical and numerical study of dual-chamber oscillating water columns on stepped bottom. Renew. Energy 75, 272–282. http://dx.doi.org/10.1016/j.renene.2014.09.050.

Rodríguez, A.A.M., Casarín, R.S., Ilzarbe, J.M.B., 2022. A 3D boundary element method for analysing the hydrodynamic performance of a land-fixed oscillating water column device. Eng. Anal. Bound. Elem. 138, 407–422. http://dx.doi.org/10.1016/j.enganabound.2022.02.014.

Sarkar, A., Chanda, A., 2022. Structural performance of a submerged bottom-mounted compound porous cylinder on the water wave interaction in the presence of a porous sea-bed. Phys. Fluids 34, http://dx.doi.org/10.1063/5.0106425.

Strauch, J., Chuchiara, D., Toldo Junior, E.E., Almeida, L.S., 2009. Padro das ondas de verao e outono no literal sul e norte do rio grande do sul. Rev. Bras. Recur. Hidr. 14, 29–37. http://dx.doi.org/10.21168/rbrh.v14n4.p29-37.

Trivedi, K., Koley, S., 2021. Mathematical modeling of breakwater-integrated oscillating water column wave energy converter devices under irregular incident waves. Renew. Energy 178, 403–419. http://dx.doi.org/10.1016/j.renene.2021.06.075.

Trivedi, K., Koley, S., 2022. Hydrodynamic performance of the dual-chamber oscillating water column device placed over the undulated sea bed. Energy Rep. 8, 480–486. http://dx.doi.org/10.1016/j.egyr.2021.11.159.

Tsai, C.C., Chang, Y.H., Hsu, T.W., 2022. Step approximation on oblique water wave scattering and breaking by variable porous breakwaters over uneven bottoms. Ocean Eng. 253, 111325. http://dx.doi.org/10.1016/j.oceaneng.2022.111325.

Wang, C., Zhang, Y., 2021. Hydrodynamic performance of an offshore oscillating water column device mounted over an immersed horizontal plate: A numerical study. Energy 222, 119964. http://dx.doi.org/10.1016/j.energy.2021.119964.

Wang, C., Zhang, Y., 2022. Performance enhancement for a dual-chamber OWC conceived from side wall effects in narrow flumes. Ocean Eng. 247, 110552. http://dx.doi.org/10.1016/j.oceaneng.2022.110552.

Wang, C., Zhang, Y., Deng, Z., 2021. Theoretical analysis on hydrodynamic performance for a dual-chamber oscillating water column device with a pitching front lip-wall. Energy 226, 120326. http://dx.doi.org/10.1016/j.energy.2021.120326.

Zheng, S., Antonini, A., Zhang, Y., Miles, J., Greaves, D., Zhu, G., Iglesias, G., 2020. Hydrodynamic performance of a multi-oscillating water column (OWC) platform. Appl. Ocean Res. 99, 102168. http://dx.doi.org/10.1016/j.apor.2020.102168.

Zheng, S., Michele, S., Liang, H., Meylan, M.H., Greaves, D., 2022. Wave power extraction from a floating elastic disk-shaped wave energy converter. J. Fluid Mech. 948, A38. http://dx.doi.org/10.1017/jfm.2022.701.

Zhu, K., Shi, H., Zheng, S., Michele, S., Cao, F., 2023. Hydrodynamic analysis of hybrid system with wind turbine and wave energy converter. Appl. Energy 350, 121745. http://dx.doi.org/10.1016/j.apenergy.2023.121745.